DEPARTMENT OF PHYSICS
UNIVERSITY OF JYVÄSKYLÄ

Determination of the fission half-life for the isotope ^{250}No

by

Federica Defranchi Bisso

A thesis presented for the degree of
Master of Science

Supervised by Professor Paul T. Greenlees

Finland, August 2016

Abstract

The aim of this thesis was to accomplish a decay spectroscopic study of ^{250}No. In particular, the research focused on determining the spontaneous fission half-life of this nucleus, giving an answer to a question arising from previous studies about the half-life of the 6^+ isomeric state. The experiment was performed in the Accelerator Laboratory of the University of Jyväskylä, using the RITU gas-filled separator and the focal plane detection spectrometer GREAT. The production of ^{250}No was achieved via the reaction ^{204}Pb(^{48}Ca,2n)^{250}No, with a beam energy of 218 MeV. The data analysis methods utilized are presented, with focus on how it was possible to extrapolate the two different components for the fission half-life. The observed fission half-life being different depending on whether the fusion reaction feeds the ground state or the isomeric state. This analysis resulted in $t_{1/2} = 3.4 \pm 0.2\mu s$ for the ground state and $t_{1/2} = 31 \pm 5\mu s$ for the isomeric 6^+ state. Furthermore, the presence of an electromagnetic branch was detected, proving that the isomeric state decays to the ground state which, then, decays by spontaneous fission.

Contents

List of Figures

List of Tables

Chapter 1

Introduction

Nuclear spectroscopy is a challenging field, especially when investigating very exotic nuclei, such as super-heavy nuclei like ^{250}No. Very short half-lives combined with low statistics make the data analysis complex besides requiring precise experimental parameters.

This work focuses on the decay spectroscopy of the even-even nucleus ^{250}No. The aim was to prove the decay mode of a 6^+ isomeric state, in particular to find whether it directly decays by fission or it decays electromagnetically to the ground state which, consequently, undergoes fission. Besides this qualitative point, both the ground-state and the isomeric state half-lives are measured, improving the accuracy with respect to previous measurements. The previous results indeed had an uncertainty of around 30% for the short component and 40-50% for the long component [4], while in this work the obtained half-lives have an uncertainty ranging from 7% for the short component to 17% for the long component.

This work is divided in four main chapters, with an additional introduction and final discussion. The first chapter lists the previous studies of ^{250}No, expressing so the physics motivation which led to run this experiment. Previous studies first identified and then characterized the isotope ^{250}No. Two different decay activities were found, one of which was attributed to the decay of an isomeric state, though without being able to understand the decay mode of this state. The second chapter describes the theoretical background necessary to understand this problem, to give an idea of the physics involved, from the exponential decay law to K-isomerism. The third chapter explains the experimental set-up conceived in order to succeed in achieving the goals of the experiment in the best possible way. The type of reaction involved, beam energy and other experimental parameters are illustrated and the RITU focal-plane apparatus is described. The last chapter, illustrates what kind of data analysis was necessary and why, which attempts were made and which option turned out to be successful in obtaining the

satisfactory results which were found.

Chapter 2

Physics motivation and previous studies

2.1 First identification of ^{250}No

The very first identification of the isotope ^{250}No was published in 1975 by Ter-Akopyan *et al.* [1]. With the aim of investigating the fission stability around the deformed shell at neutron number N=152, they bombarded a ^{233}U target with a ^{22}Ne beam at an energy of 120 MeV. This energy was chosen to match the predicted peak of the excitation energy for the 5n channel, i.e. to the reaction ^{233}U(^{22}Ne,5n)^{250}No. The region of the N=152 shell is of particular interest to understand how this shell affects the half-life of the super-heavy elements (see figure 2.1).

In this experiment, they detected a fission activity with a measured half-life $t_{1/2}$=0.25$\pm$0.05 ms and production cross section of about 1.5 nb [1]. This activity could be attributed to an isotope with Z=102 and N=148 because, among the reactions ^{233}U(^{22}Ne,$x$$n$), the 5$n$ channel is predominant at the chosen bombarding energy. The 4n channel had a similar cross section, but ^{251}No was well known to undergo α-decay with a much longer half-life. Also other possible candidates were excluded because they had very different half-lives from the one detected. Since the α-decay half-life for ^{250}No had been estimated to be larger than 0.03 ms, the principal mode of decay for this isotope was attributed to spontaneous fission [1].

Further information about ^{250}No became available in 2001, when Oganessian *et al*. published a paper [2] reporting the results obtained in an experiment, run at the Dubna gas-filled separator, which they performed in order to study the excitation energies and maximum cross sections for the reactions ^{206}Pb(^{48}Ca,1-4n) and ^{204,207,208}Pb(^{48}Ca,2n). In these reactions both the target and the projectile have proton and neutron numbers near or at a spherical shell. Furthermore, the compound nuclei have neutron numbers around the deformed N=152 shell. As

stated before, this feature is of particular interest to understand how this shell affects structure and properties of heavy nuclei.

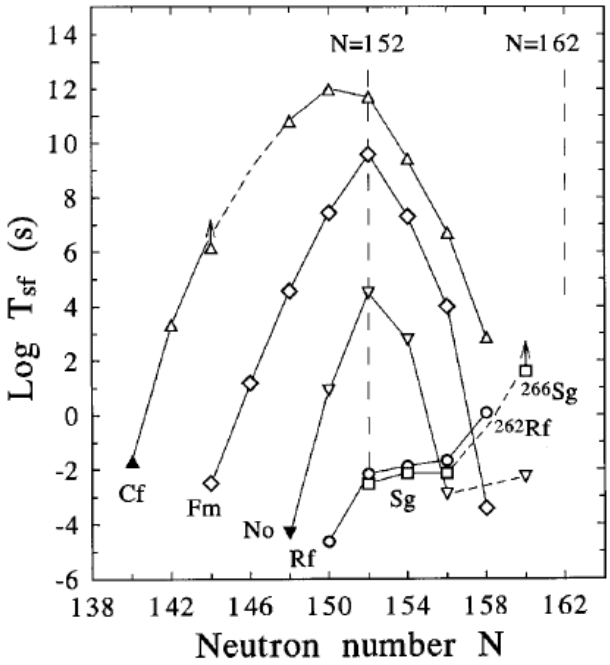

Figure 2.1: Partial spontaneous fission half-life of even-even nuclei with proton number from 98 to 106. Solid symbols show new results from Oganessian for ^{238}Cf and ^{250}No while other experimental data are taken from previous studies, see Refs. 14,21,22,27,28 of [2]. It should be noted how the half-life drops moving away from the N=152 shell.

While bombarding ^{206}Pb with ^{48}Ca, they observed ten events of a new spontaneous fission activity, with a half-life of $t_{1/2} = 26^{-6}_{+12}$ μs [2]. Both the excitation function and the position of the maximum cross section, led to the conclusion that they were in fact observing the reaction ^{206}Pb(^{48}Ca,4n)^{250}No. With this half-life, they extrapolated a cross section of $0.26^{-0.13}_{+0.19}$ nb for incident energy 242.5 MeV.

At this point, in order to investigate further into the properties of ^{250}No, they bombarded a ^{204}Pb target with a ^{48}Ca beam, in an energy range corresponding to the predicted maximum cross section for the 2n channel. With this reaction, they detected another eleven events showing a half-life of $t_{1/2} = 46^{-11}_{+19}$ μs. For this second reaction the cross section was found to be $9.5^{-4.9}_{+7.6}$ nb at an energy of 216.7 MeV.

Therefore, for the 21 events detected with both reactions, the spontaneous fission half-life of ^{250}No determined was $t_{1/2} = 36^{-6}_{+11}$ μs [2]. This is considerably shorter than that of the next even-even No isotope, as can be seen in figure

2.1. Specifically, it is 5×10^8 times smaller than the half-life of ^{254}No [2], which is at the N=152 shell. Nobelium presents the strongest change in spontaneous fission half-life among all the even-Z nuclei, and Oganessian attributes this to the rapid disappearance of the macroscopic fission barrier and the consequent increase in the shell effect on the stability of the nucleus, comparing to lightest elements. Moreover, the measured cross-section for the reaction ^{204}Pb(^{48}Ca,2n)^{250}No strongly deviates from the predicted one and this led the way to further investigations.

2.2 Further studies

Further results concerning ^{250}No were published in 2003 by Belozerov *et. al* [3]. This study focused on the synthesis of the neutron-deficient nobelium isotopes formed in the ^{204,206,208}Pb(^{44,48}Ca,$x n$) reactions.

In this experiment, the ^{48}Ca+^{206,208}Pb reactions were first used to test the transmission of the separator and to calibrate the focal plane for energy and position. While performing the ^{48}Ca+^{206}Pb reaction, with a beam energy of 234.5$\pm$ 2.3 MeV in the laboratory frame, they detected two events with half-life $t_{1/2} = 5.9^{-2.3}_{+10.7}$ μs [3] which they assigned to the 4n channel, hence to the decay of ^{250}No.

Proceeding to the ^{48}Ca + ^{204}Pb reaction, with energies 217.8, 223.6 and 229.4 MeV, activities were found with three different half-life values. More specifically, 42 events with $t_{1/2} = 5.9^{-0.8}_{+1.1}$ μs, 22 events with $t_{1/2} = 54.2^{-9.5}_{+14.7}$ μs and 10 events with $t_{1/2} = 2.4^{-0.6}_{+1.1}$ s were detected [3], and these results are illustrated in figure 2.2. The latter ten events were assigned to ^{252}No formed in the reaction of ^{48}Ca with the contamination of ^{206}Pb present in the target. The 5.9 μs activity was assigned to the decay of ^{250}No while the 54.2 μs one tentatively to the odd-mass isotope ^{249}No.

The experiment then moved to the reaction ^{44}Ca+^{208}Pb using three different beam energies: 216.8, 212.1 and 205 MeV. In this case thirteen events, eleven with $t_{1/2} = 5.4^{-1.3}_{+2.3}$ μs and two with $t_{1/2} = 48^{-19}_{+87}$ μs, were detected [3]. In these values we can recognize the ones previously obtained in the reaction ^{48}Ca+^{204}Pb. Furthermore, in the reaction ^{44}Ca+^{206}Pb with beam energy of 214.7 MeV one event with life time 29 μs was detected, which was attributed to the reaction of ^{44}Ca with the contamination of ^{208}Pb in the target.

In order to estimate the mass of the detected spontaneous fission activities, recoil-fission correlation, position of the implanted recoil and corresponding time-of-flight techniques were used. The results of this mass identification can

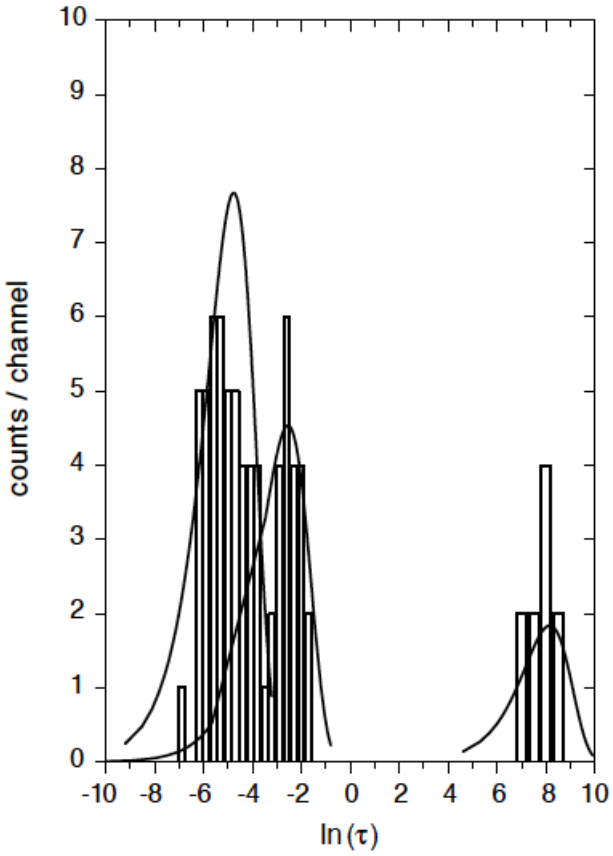

Figure 2.2: Logarithm of the life-times in ms, ln(τ), collected in the ^{48}Ca+^{204}Pb reaction. The three different components corresponding to half-lives $5.9^{-0.8}_{+1.1}$ μs, $54.2^{-9.5}_{+14.7}$ μs and $2.4^{-0.6}_{+1.1}$ s can be clearly identified [3].

be seen in figure 2.3. To sum up, a total of 56 events were assigned to ^{250}No, with a half-life $t_{1/2} = 5.6^{-0.7}_{+0.9}$ μs and a total of 24 events to ^{249}No, with a half-life $t_{1/2} = 54^{-9.2}_{+13.9}$ μs [3]. Comparing their results to the ones published in [1] and [2] they suggest that the difference is due to the longer dead time in the previous studies, which did not allow half-lives shorter than 10 μs to be detected.

Despite the improvements achieved, the authors of [3] are not certain about the attribution of the 54 μs activity to ^{249}No decay, since the measured yield is comparable to the one obtained in [2] for $t_{1/2} = 36^{-6}_{+11}$ μs, but five times lower than the one of $t_{1/2} = 5.6^{-0.7}_{+0.9}$ μs. Thus, they state that the $t_{1/2} = 54^{-9.2}_{+13.9}$ μs activity could possibly be emitted by an isomeric state of ^{250}No. This puzzling question opens the way to further studies, necessary to understand with certainty the real origin of the activity.

Further investigations were made and published in 2006 by Peterson *et. al*

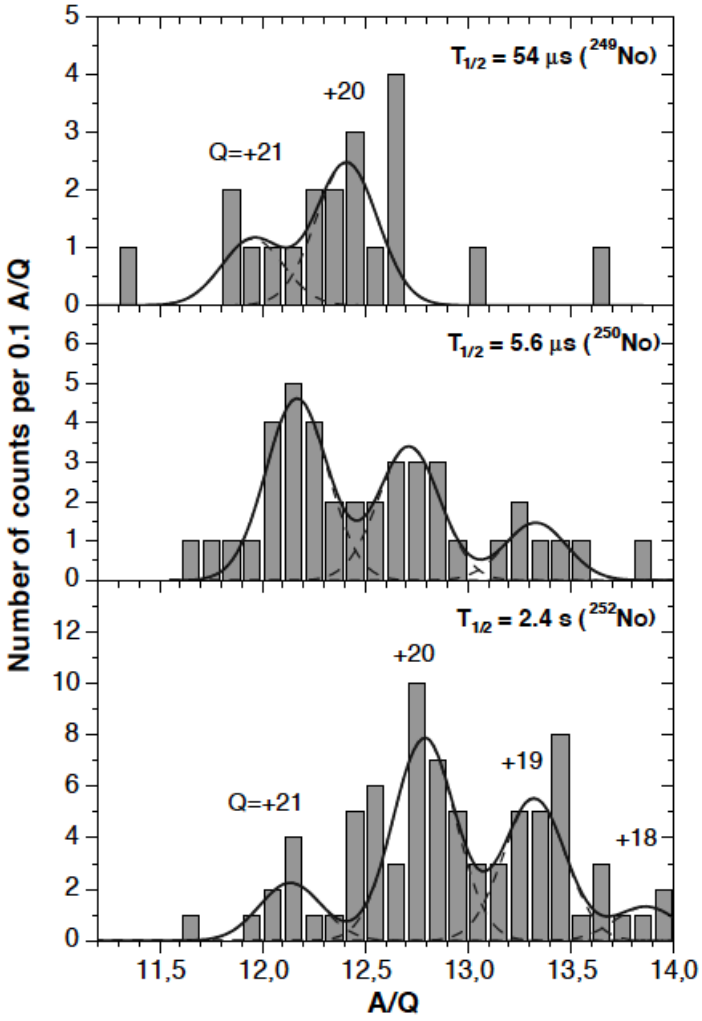

Figure 2.3: Mass over charge distribution for the activities 5.6 μs, 54 μs and 2.4 s observed in the reactions ^{44,48}Ca+^{204,206}Pb. Experimental data were fitted with a multi-Gaussian (lines), in the first and third panel the assumed charge states for the recoils are indicated [3].

in [4]. With the aid of the Fragment Mass Analyzer (FMA) at the ATLAS facility, they were able to associate each measured decay lifetime with a specific mass. They used highly enriched targets of ^{204}Pb, in order to account for the much higher cross-section for the (^{48}Ca,2n) reaction for the isotopes ^{206,207,208}Pb and to minimize their contribution. Even with this precaution, these impurities caused up to 15% of the total residue rate.

Using a correlation time of 500 μs, a total of 158 recoil-fission correlations were detected [4], from which they extracted two different half-life components, the shorter equal to $t_{1/2} = 3.7^{-0.8}_{+1.1}$ μs and the longer to $t_{1/2} = 43^{-15}_{+22}$ μs. They also derived the production cross sections to be 12^{-4}_{+18} nb for the shorter lived activity

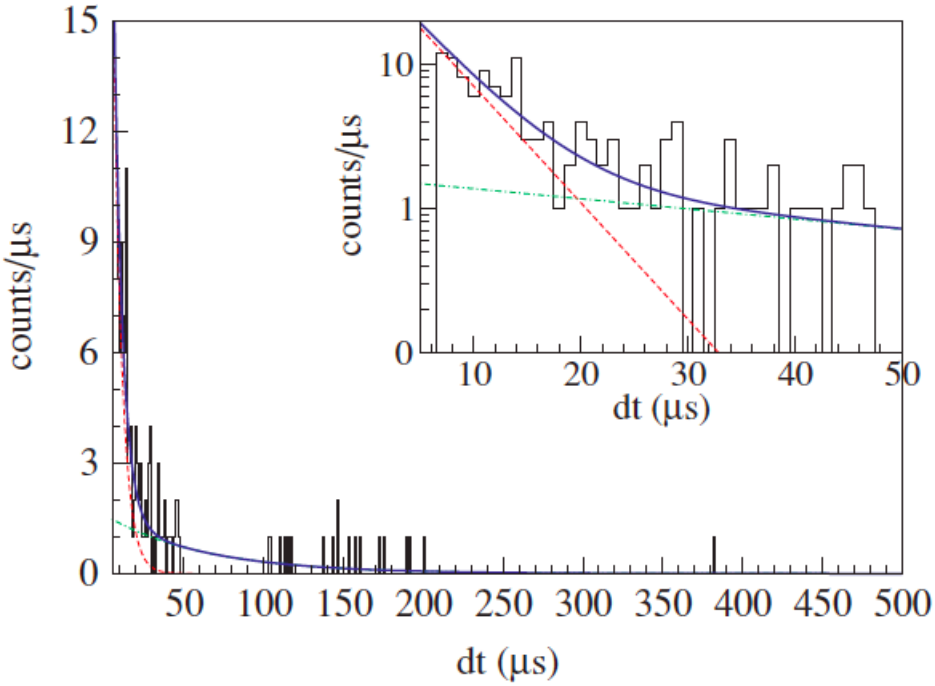

Figure 2.4: Decay timespectrum for the 158 recoil-fission correlation events observed by Peterson et al. [4]. The inset focuses on the first 50 μs. The dashed red line and the dot-dashed green line represent the contributions from the individual components with half-life respectively 3.7 and 43 μs. The solid blue line is the combination of the previous two.

and 5^{-2}_{+3} nb for the longer lived one. The decay spectrum for all these events can be seen in figure 2.4. The mass identification was done at the focal plane of the FMA, and the results are shown in figure 2.5.

In light of the mass analysis, both half-life components were attributed to ^{250}No. Given that ^{250}No is an even-even nucleus the ground state will have a 0^+ configuration. Assuming its structure to be similar to the neighboring even-even isotopes ^{252}No and ^{254}No, then ^{250}No will present a prolate shape, implying the lowest excited states to be forming a collective rotational band. The ratio of the calculated cross sections is $\sigma_{\text{short}}/\sigma_{\text{long}}$ = 2.45, which means that about 29% of the events feeds the state with the longer half-life. Comparing this to other results about isomeric states in ^{254}No and ^{250}Fm, in this study it is suggested that the short component ($t_{1/2}$=3.7 μs), with higher cross section, is to be attributed to the ground state, whilst the less intense long component ($t_{1/2}$ = 43 μs) corresponds to an isomeric state. All this considered, and given theoretical predictions obtained using multi-quasiparticle blocking calculations, a good candidate for the isomeric state is a level at 1050 keV with configuration $\nu^2(5/2^+[622],7/2^+[624])_{6^+}$, i.e. K^π=6^+ [4].

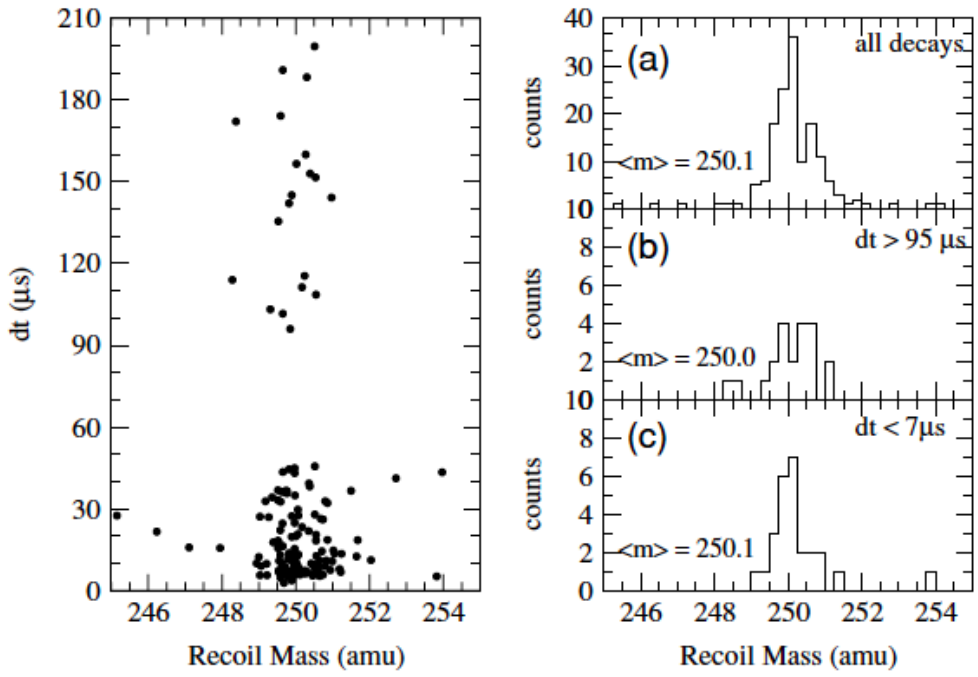

Figure 2.5: Mass numbers of the nuclides associated with spontaneous fission decays detected by Peterson *et al.* In the left-hand panel, decay times versus mass is plotted. In the right-hand panels, they project to the mass axis for, from top to bottom, all decays, only long and mostly short component [4].

In this experiment, it was not possible to distinguish whether the detected longer activity originates from the isomeric state directly fissioning, or from the isomeric K-forbidden γ-decaying to the ground state which then fissions itself. Hence, this question remains unanswered and the present work aims to solve this matter.

Chapter 3

Theoretical aspects

3.1 Radioactive decay and nuclear reactions

The spontaneous emission of radiation or particles from a nucleus is called *radioactivity*. A decaying nucleus can emit nucleons (protons, neutrons, β and α particles) and electromagnetic radiation (γ rays), or it can fission. These processes can be spontaneous or, in case of fission, induced.

All these decays obey the following exponential law

$$N(t) = N_0 \cdot e^{-\lambda \cdot t} \tag{3.1}$$

where *N(t)* is the number of atoms at a time t, N_0 at a time *t=0* and λ is the decay constant, characteristic of the specific isotope. From this constant the *half-life* can be determined via the relation

$$t_{1/2} = \frac{\ln 2}{\lambda} = \tau \ln 2 \tag{3.2}$$

Where τ is the *life-time* and the *half-life* $t_{1/2}$ gives the time necessary for half of the nuclei to decay.

A nuclear reaction of the type A + a $\longrightarrow$ B + b is usually written in the form A(a,b)B, where conventionally A is the heavy target, a is the light projectile, b is the light product and B is the heavy product. Any reaction is characterized by the Q value, which is

$$Q = (m_{initial} - m_{final}) \cdot c^2 = (m_A + m_a - m_b - m_B) \cdot c^2 \tag{3.3}$$

Where m_A, m_a, m_b and m_B are the atomic masses of, correspondingly, the target, the projectile, the light product and the heavy product.

When the Q value is negative the reaction is *endoergic*, which means the reaction occurs via absorption of energy, whilst when Q is positive the reaction is *exoergic*.

In a fusion evaporation reaction, like the kind used in this experiment, a highly energetic projectile is used to bombard a target and, overcoming the Coulomb barrier, cause a fusion reaction. Immediately after this fusion occurred, the so formed compound nucleus emits ("evaporates") nucleons. The final product is known as a *fusion-evaporation residue*.

3.2 Nuclear fission and liquid drop model

We talk about nuclear *fission* when a nucleus breaks apart and splits into two smaller parts. This process originates in a heavy nucleus from the competition between the nuclear force, binding nucleons together, and the Coulomb repulsion, pushing protons away from each other. Fission can be spontaneous or induced by particles (neutrons, photons, electrons, protons or heavy ions) bombardment.

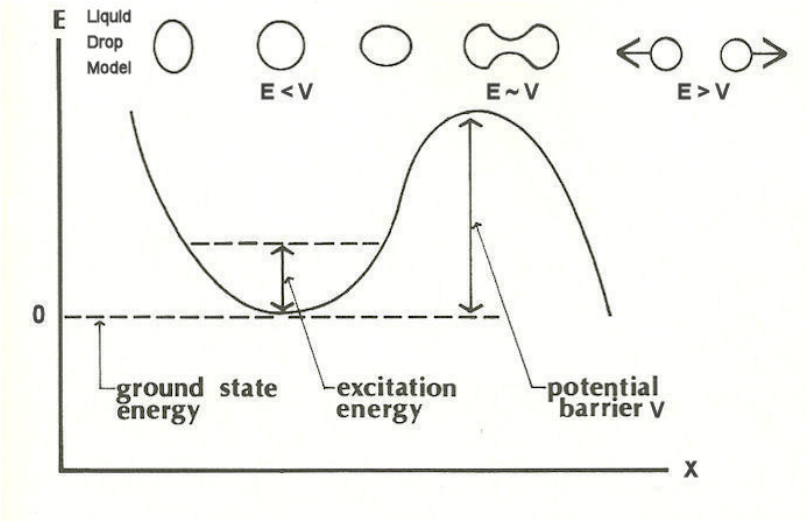

Figure 3.1: Fission barrier and deformation according to the liquid-drop model. Not considering the quantum tunneling, we can see that a nucleus can fission if and only if its energy overcomes the barrier height. [21].

Spontaneous fission is possible when the system goes from a less tightly bound system to a more tightly bound one, in other words when the binding energy of the parent nucleus is less than the sum of the binding energies of the daughters. Reasoning in this way, fission should be very likely while going towards less bound nuclei in the binding energy curve (figure 3.3). In reality fission

does not compete successfully with other decay modes, such as α-decay, until nuclei with mass of about 250 or heavier [19]. The nucleus, indeed, must have enough energy to surmount the fission barrier; the barrier height to overcome is called *activation energy*. For nuclides with $A < 230$ the activation energy is pretty large, and fission can happen only if we provide enough energy. From mass A $\sim$ 250 on, the activation energy starts having also negative values and nuclides can fission spontaneously.

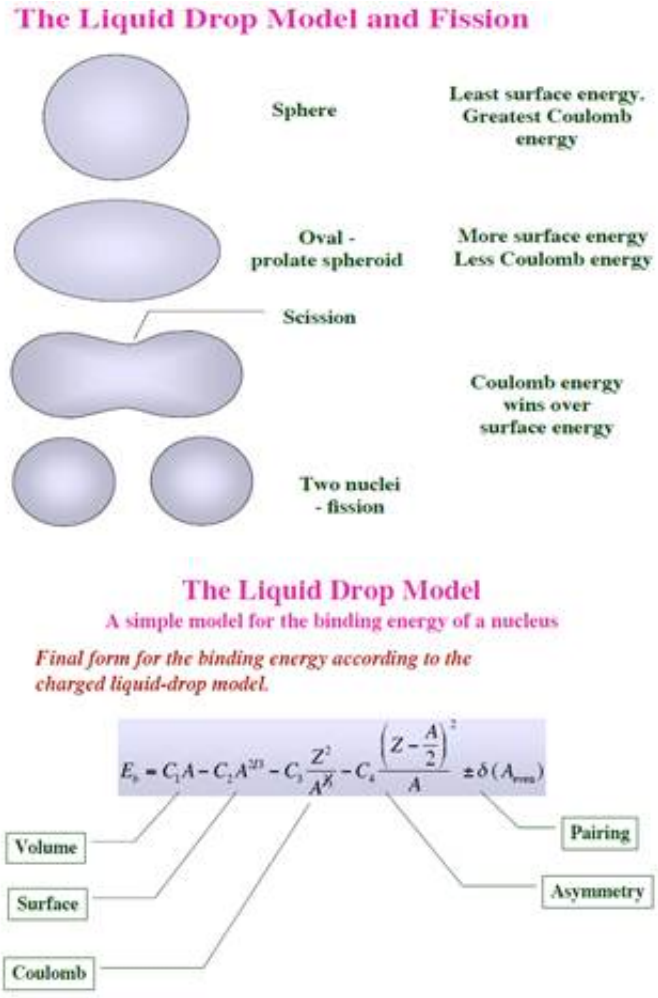

Figure 3.2: Scheme for the LDM of fission (upper) and binding energy of a nuclei (lower). It can be seen how the process leading to the separation of two fragments from one nucleus depends on a competition between the surface term and the Coulomb term [14].

In the LDM (Liquid Drop Model) the binding energy is expressed with the semi-empirical mass formula, with the following expression:

$$B = a_v A - a_s A^{2/3} - a_c Z(Z-1)A^{-1/3} - a_{sym}\frac{(A-2Z)^2}{A} + \delta \tag{3.4}$$

Where A is the mass number, Z is the proton number, and a_v, a_s, a_c, a_{sym}, and δ are parameters chosen to fit the experimental data, hence the term "semi-empirical". In this formula, the first three terms (volume, surface and Coulomb terms) deal with the nucleus as a whole, while the last two (symmetry and pairing terms) refer more to individual nucleons. The binding energy per nucleon as a function of the mass number A can be seen in figure 3.3.

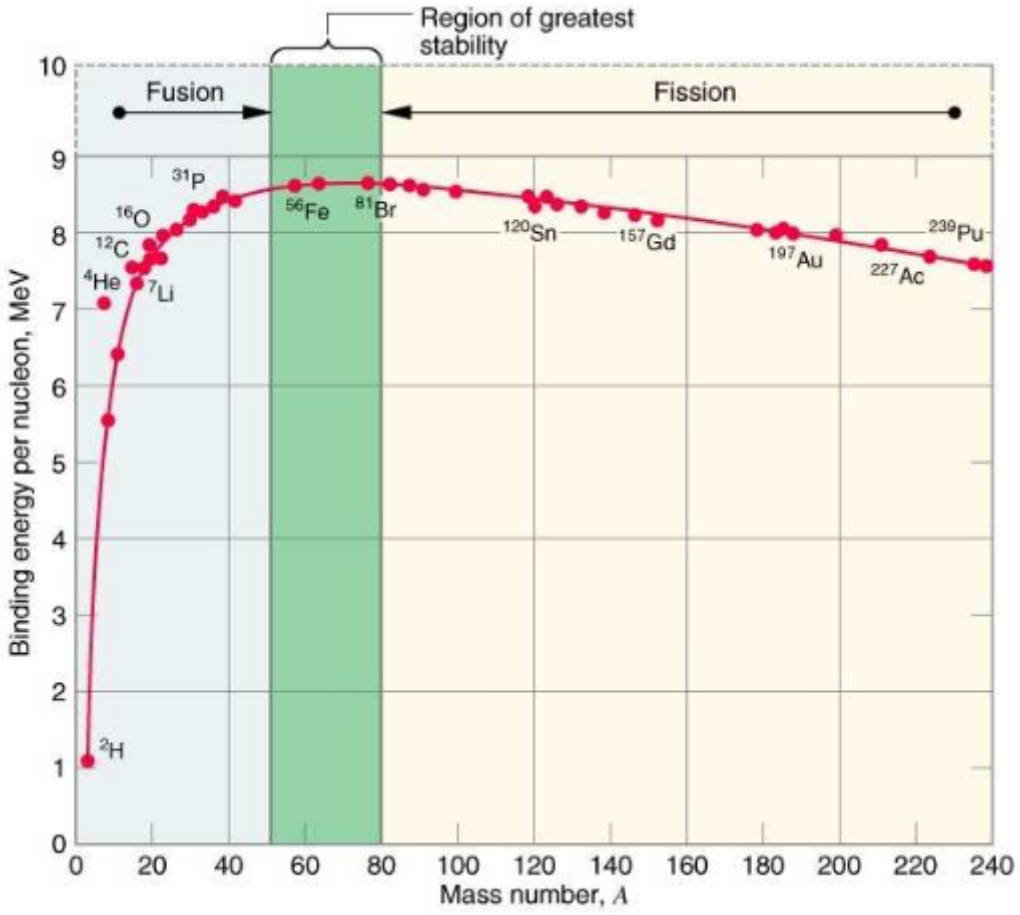

Figure 3.3: Binding energy per nucleon in MeV as a function of the mass number A. The solid line is the theoretical binding energies obtained with the semi-empirical mass formula, while the dots represent the experimental values. Note how the maximum is around the doubly magic isotope ^{56}Fe [22].

Although the LDM fails when trying to explain some nuclear features, it succeeds in describing nuclear fission. Indeed, as we can see in figure 3.1, while approaching the barrier, the deformation increases, causing the surface term to

increase, whilst the Coulomb term decreases, altogether leading to a decrease in the total binding energy so that the two globes in figure 3.1 can eventually separate. This competition between surface and Coulomb term occurring with deformation is also shown in figure 3.2.

3.3 Nuclear shell model

As mentioned above, some nuclear features can not be explained with the LDM, for example the separation energy for protons (S_p, S_{2p}) and neutrons (S_n, S_{2n}). Experimental data show sharp drops around certain proton and neutron numbers, suggesting a shell structure. In order to explain this behavior, several attempts were made to describe the motion of an individual nucleon in a nucleus and various potentials were tried.

The best choice turned out to be the Woods-Saxon potential, which is expressed with the relation:

$$V(r) = \frac{-V_0}{1 + e^{\frac{r - R_{ave}}{a}}}, \tag{3.5}$$

where R_{ave} gives the mean radius, a the skin thickness of the nucleus and V_0 is the depth of the potential well, which is chosen in order to match the experimental separation energies.

This potential reproduces the first three closed shells (magic numbers 2, 8, 20), but the higher magic numbers are still missing, as is shown in figure 3.4. The issue was solved by Maria Goeppert-Mayer [13], who for this reason won, jointly with J. Hans D. Jensen and Eugene P. Wigner, the Nobel prize for physics in 1963. The solution consisted in adding to this potential a *spin-orbit* interaction, dependent on the orbital angular momentum quantum number l, the spin quantum number s, and the total angular momentum of the orbital $j = l \pm s$ as follows:

$$< l \bullet s >= \frac{1}{2}[j(j+1) - l(l+1) - s(s+1)]\hbar^2 \tag{3.6}$$

The effect of this correction, how it changes the predicted energy levels and causes the correct magic numbers to arise, is shown in figure 3.4.

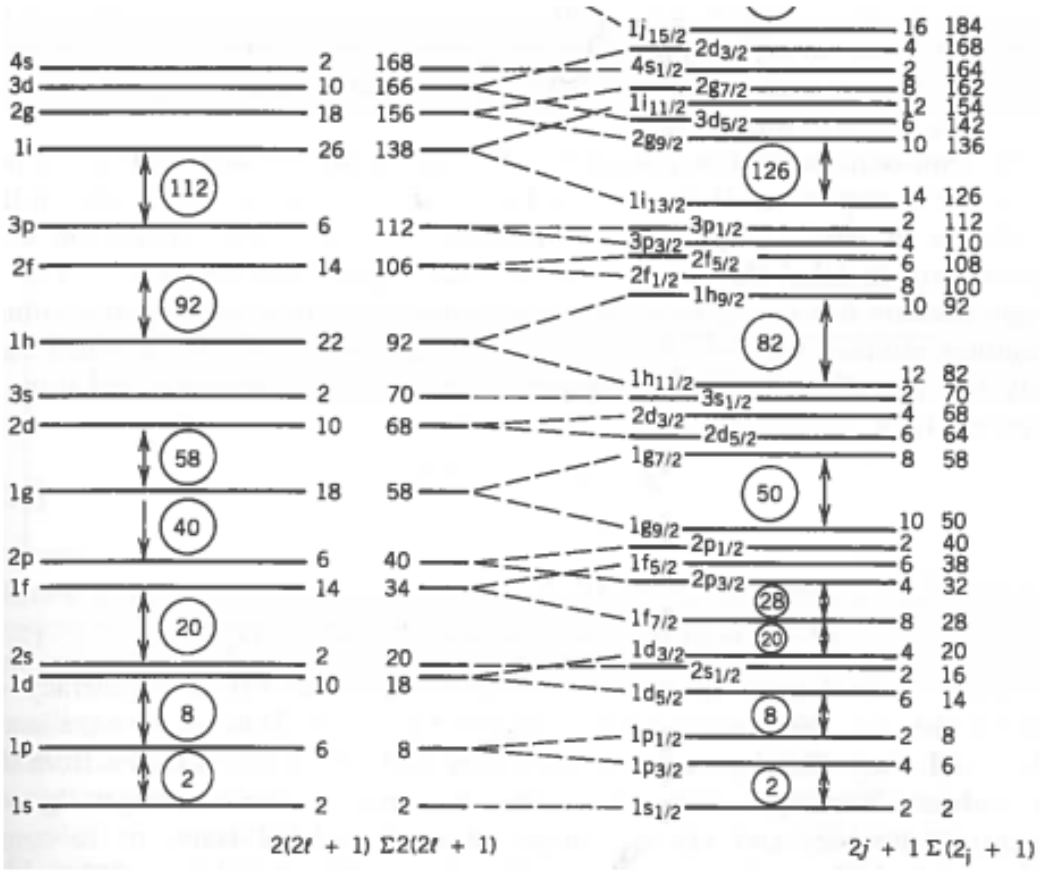

Figure 3.4: Calculated energy levels from Woods-Saxon potential (left hand side) and the same potential with the spin-orbit correction (right hand side). The shell structure is evident, circled numbers represent the magic numbers corresponding to closed shells, while numbers on the left give the maximum amount of protons/neutrons which can be in each state. Notice how the spin-orbit correction makes all the empirically observed magic numbers arise. Reprinted from figure 5.6 of [19].

3.4 Deformed nuclei and Nilsson model

As anticipated in the previous section, the spherical shell model is not a good model if we have to deal with deformed nuclei. With *deformed nucleus* we mean a nucleus with shape importantly different from spherical, more specifically a shape resembling an ellipsoid of revolution. For an electric quadrupole deformation, the surface of deformed nuclei can be described with

$$R(\theta,\phi) = R_{ave}[1 + \beta Y_{20}(\theta,\phi)] \tag{3.7}$$

Where $Y_{20}(\theta,\phi)$ is the spherical harmonics of order two and β is the *deformation parameter*, which depends on the eccentricity as

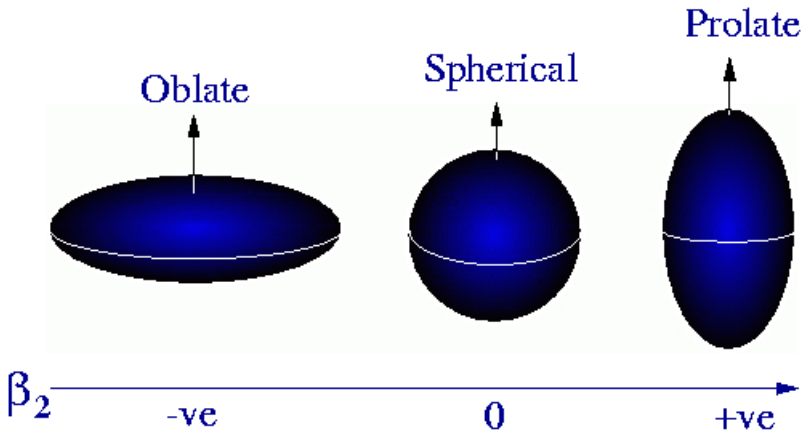

Figure 3.5: Oblate, spherical and prolate shapes, ordered with respect to the deformation parameter values, from negative (oblate) to positive (prolate) going through zero (spherical). The arrow also indicates the symmetry axis. Taken from [17].

$$\beta = \frac{4}{3}\sqrt{\frac{\pi}{5}}\frac{\Delta R}{R_{ave}}, \tag{3.8}$$

where ΔR is the difference between the two semi-axis of the ellipse and $R_{ave} = R_0 A^{1/3}$. When $\beta > 0$ the nucleus has a *prolate* shape while, when $\beta < 0$, it has an *oblate* shape. These nuclear deformations are illustrated in figure 3.5.

In the spherical shell model (described in section 3.3) each level has a degeneracy of *2j+1*, which means that there are *2j+1* possible orientations of **j** and they all are equivalent in energy. In case of deformed nuclei this is not true anymore; indeed, if the potential is not spherical the orientation of the orbital actually affects the energy of the level.

A major tool to deal with deformed nuclei is the *Nilsson model*. In this model, we do not refer to **j** anymore, as it is not a good quantum number in this case, but rather to its projection along the axis of symmetry, which is usually denoted by Ω. An orbital with $j = \frac{7}{2}$, for example the $1f_{7/2}$ orbital, will have eight different possibilities for Ω, from $-\frac{7}{2}$ to $+\frac{7}{2}$. The components $+\Omega$ and $-\Omega$ have the same energy, therefore each Nilsson level will have a degeneracy of 2. Following our previous example, we can state that the spherical level $1f_{7/2}$ will split into four Nilsson levels.

A Nilsson level is labeled via four different quantum numbers, which are expressed in figure 3.6, as follows:

$$\Omega^{\pi}[Nn_z\Lambda] \tag{3.9}$$

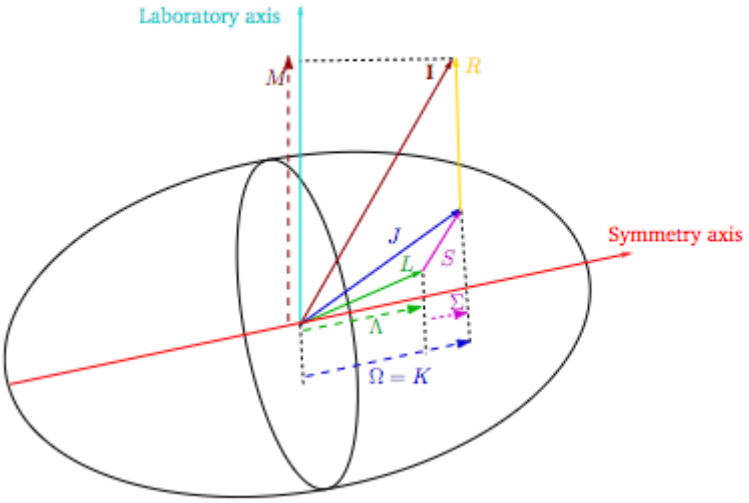

Figure 3.6: Single particle coupling to core and Nilsson quantum numbers. Being Ω the projection of the total angular momentum **J**, which is given by the vectorial sum of the spin **S** and orbital angular momentum **L**, and being Λ and Σ the projections of, correspondingly, orbital angular momentum and spin, it can be noted how Ω=Λ+Σ holds. **R** is the difference between **I** and **J**. Taken from [18].

where Ω has already been defined and π is the parity. Inside the brackets there are the principal quantum number N, the number of nodes of the wave function along the symmetry axis n_z and the component of orbital angular momentum along the symmetry axis Λ. Besides, if we denote the projection of the spin s with Σ, we see that Ω=Λ+Σ.

A typical Nilsson diagram displays the levels energy as a function of the deformation parameter β, an example is shown in figure 3.7. We can see how, due to Pauli exclusion principle, lines with the same Ω can not cross. In case of collective states, the wave function can be written as a mixture of the single-particle wave functions. In this case, the projection of the total angular momentum of the nucleus $\boldsymbol{I}$ onto the symmetry axisis conventionally indicated with $\boldsymbol{K}$. Therefore we can write:

$$K = \sum_i \Omega_i \tag{3.10}$$

3.5 K-isomerism

A nuclear *isomer* is defined as a metastable nuclear excited state, in another words we can say it is an excited state with a long half-life. There is no strict limit to the

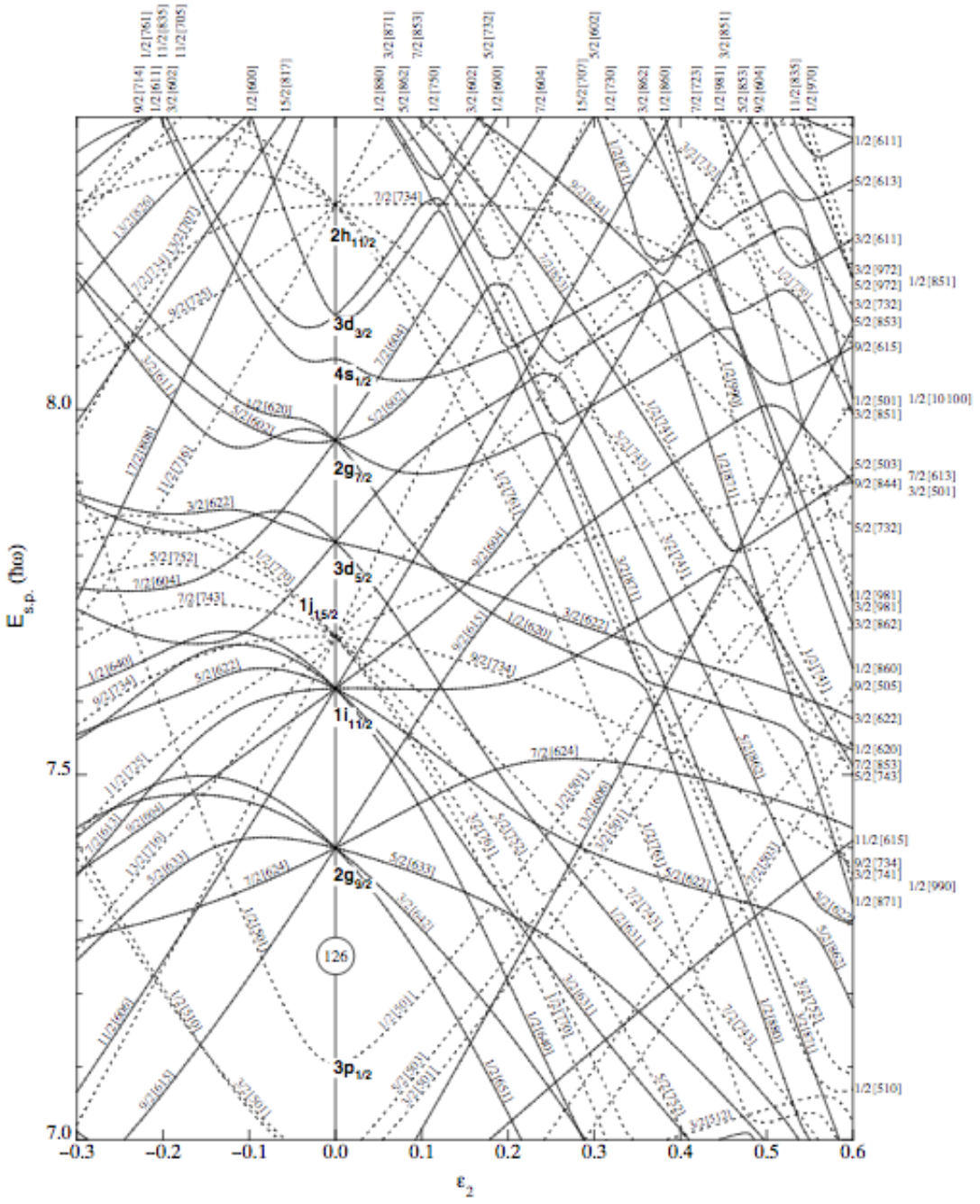

Figure 3.7: Nilsson diagram for $N \geq 114$. Single particle energy levels as a function of deformation parameter. At $\beta = 0$ the Nilsson levels degenerate into the spherical level, increasing then their splitting going far from sphericity. [24].

meaning of ”long”, but we assume it to be longer than the usual non-isomeric excited state half-life, which is around tens to hundreds of picoseconds. Conventionally, the limit of an isomer’s half-life can be set at 1 ns. A nuclear isomer

can also be seen as a state with significantly different structure than those that it decays to, feature which may results in a ”long” lifetime.

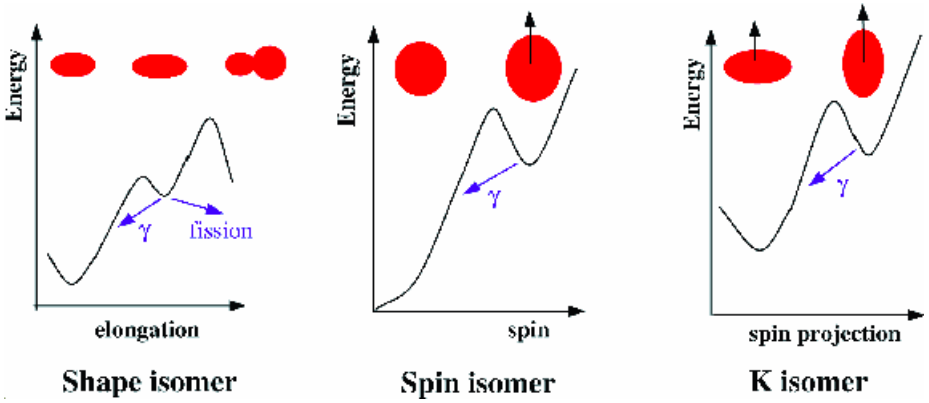

Figure 3.8: Classes of nuclear isomers. From left to right: shape trap, spin trap and K trap. [25].

Nuclear isomers are usually classified in three classes: *spin traps*, *shape isomers* and *K-traps*, illustrated schematically in figure 3.8.

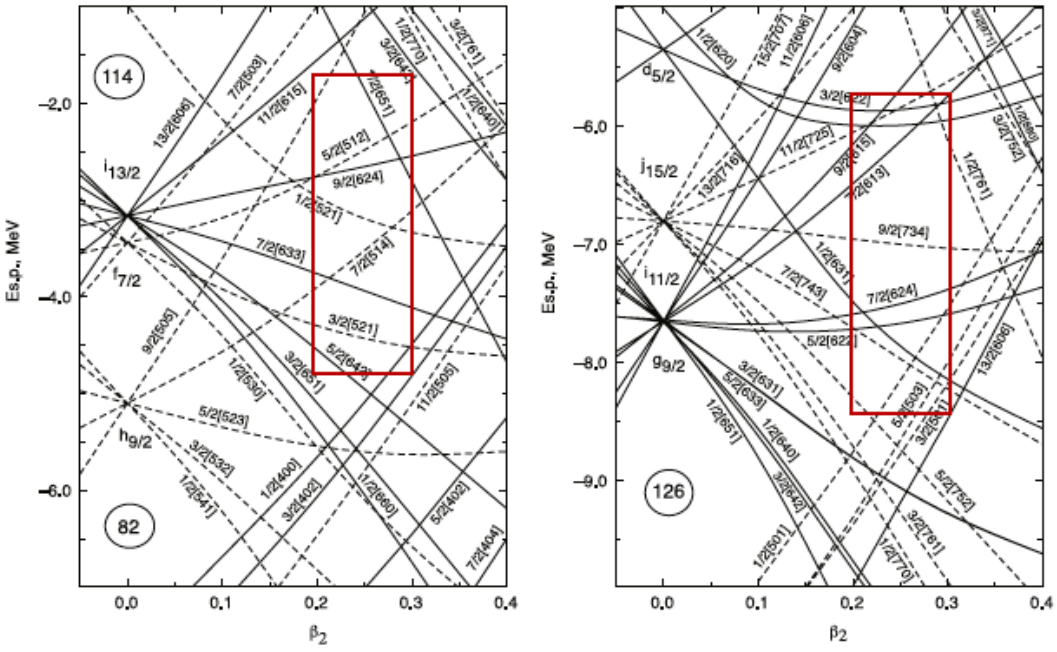

Figure 3.9: Nilsson diagram for protons (left hand side) and neutrons (right hand side) in the mass region $A \sim 250$, of interest of this work. The red boxes indicate the main orbits of interest for the formation of K-isomeric states. Taken from figure 3 in [5].

Spin traps are when a nucleus can only decay to states with big difference in spin, i.e. when only high multipolarity transitions can occur while low multipolarity transitions are forbidden.

A shape isomer occurs for a nucleus when the binding energy curve has a second minimum at a large deformation.

In deformed nuclei, the only quantum numbers which are preserved in a transition are parity π and projection of total angular momentum K. An electromagnetic transition, in order to be allowed, has to fulfill the condition $\lambda \geq \Delta K$, where λ is the multipolarity of the transition. Hence, if the change in K between initial and final configuration ΔK is large, then a *K-trap* occurs.

There are specific proton and neutron numbers of interest for the formation of K isomers in prolate-deformed nuclei. These are expressed, for the mass region involved in the present work, in figure 3.9.

For the subject of the present work, theoretical calculations [30] predict a favored state at 1050 keV with a configuration $\nu^2(5/2^+[622], 7/2^+[624])_{6^+}$. This configuration happens to be the same as the isotone ^{244}Cm, shown in figure 3.10, which then can be taken as a guidance to understand ^{250}No. Indeed in ^{244}Cm a K=6 isomeric-state is present, decaying electromagnetically to the ground state and with a different half-life.

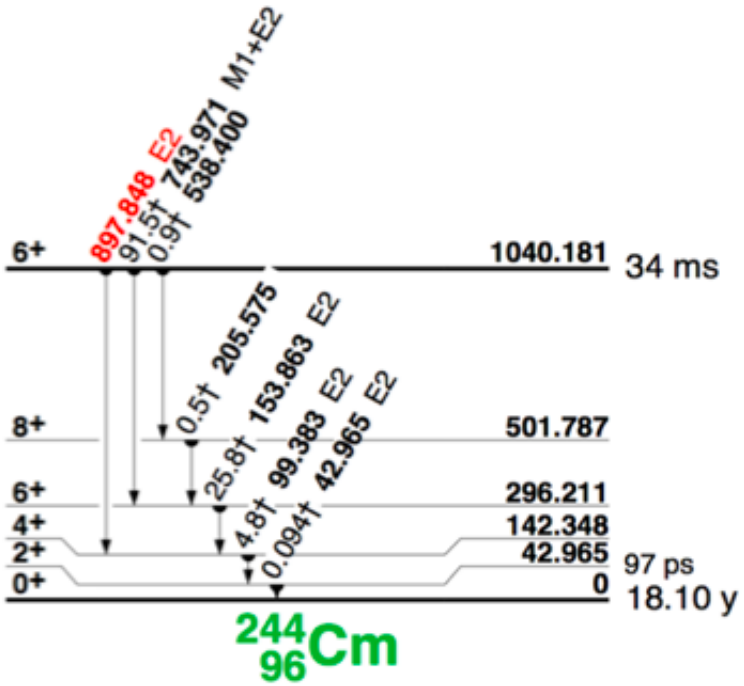

Figure 3.10: Energy level for ^{244}Cm, isotone which can be taken into guidance to understand the ^{250}No. It can be seen how a K=6 isomeric state is present, as well as two different half-lives and the electromagnetic decay from the isomeric-state to the ground-state. [16].

Also, Delaroche *et al.* [10] performed a calculation of the two quasi-particles

excitation energies for the isotonic chain N=148 for elements between plutonium and nobelium. The results of this calculation are illustrated in figure 3.11. Observing this image, we can see how the energies for all of the isotones do not change considerably, differing only for about 100 keV. All this considered, it is possible to assign the longer-lived activity to a $K^{\pi} = 6^{+}$ isomer, and we expect the energy of his state to be at 1050 ± 100 keV.

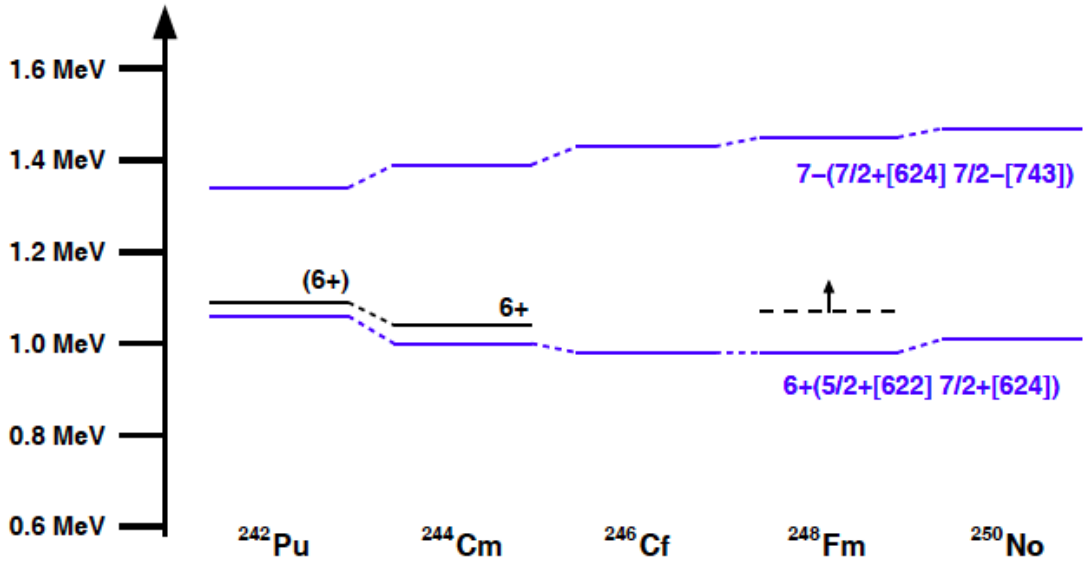

Figure 3.11: Energies of K-isomers in the N=148 isotonic chain. The blue levels are calculated in [10] while the black levels are experimental values obtained in [11] and [12]. Taken from [16].

Chapter 4

Experimental apparatus

4.1 Reaction and experimental parameters

In order to achieve a successful decay spectroscopic study of ^{250}No, the reaction used was ^{204}Pb(^{48}Ca, $2n$)^{250}No. The kind of reaction employed is known as *fusion-evaporation reaction*. In this kind of reaction, straight after the fusion occurs in the target chamber, the compound nucleus ^{252}No* promptly evaporates neutrons (specifically two neutrons in the $2n$ channel) and then the fusion-evaporation product (known as a recoil) travels through the separator RITU and reaches the focal plane, implanting into the Double Strip Silicon Detector (DSSD). The whole apparatus is illustrated in figure 4.1.

The target employed was highly enriched ^{204}Pb and ^{204}PbS, with a carbon foil first facing the beam and then in downstream position. $^{\text{PbS}}$ is a lead sulphide and it is used for its higher melting point and its better resistance to a high intensity beam. The target's structure is better described in table 4.1.

Table 4.1: Structure of the target employed in the experiment, with thicknesses of all the components. The Carbon foil was facing the beam (upstream direction) during the first part of the experiment and then it was moved to a downstream position.

Composition	**Thickness**
C	40 $\mu g/cm^2$
^{204}PbS	533 $\mu g/cm^2$
^{204}Pb	460 $\mu g/cm^2$

The bombarding ^{48}Ca beam had an energy of 218 MeV in the laboratory frame. The intensity was asked to be as high as possible, but during the experiment it oscillated around a value of 100 pnA for most of the detection time. The

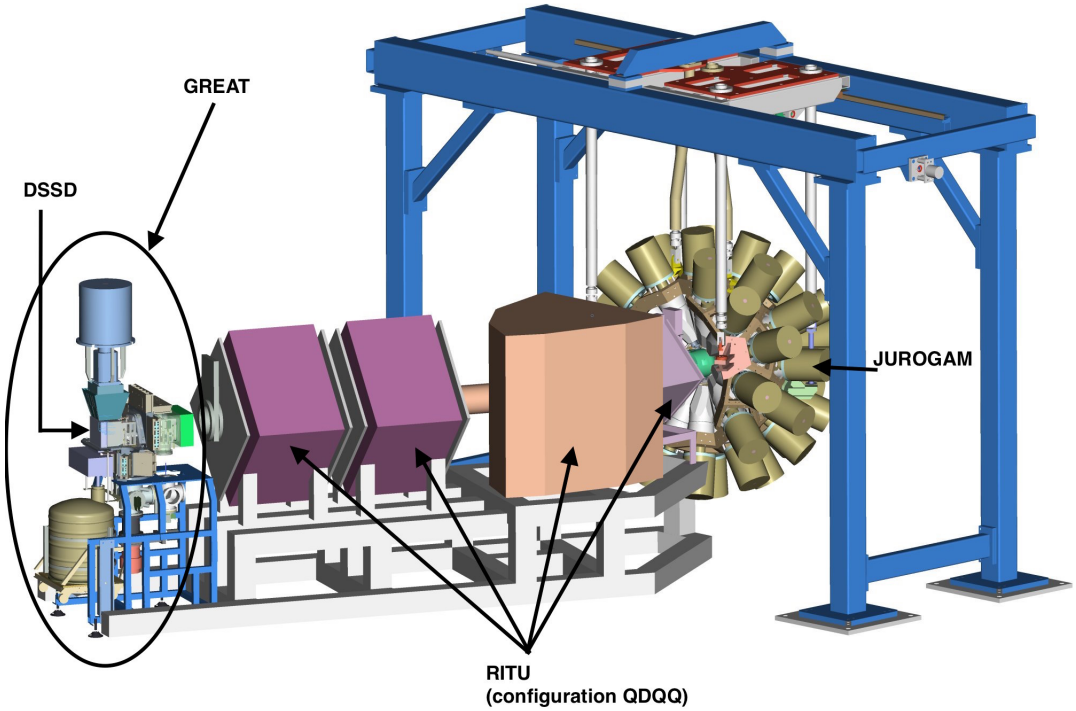

Figure 4.1: Jurogam-RITU-GREAT apparatus. The fusion evaporation product travels from the point of creation (target chamber in the center of Jurogam) through the Gas Filled Recoil Separator RITU (with magnetic configuration Quadrupole Dipole Quadrupole Quadrupole) to where it implants (focal plane) and is detected (DSSD of GREAT) [27].

carbon foil was used both downstream and upstream, and also on both sides of the target, in order to reduce the sputtering.

The experimentally obtained fusion evaporation cross-section [3] and the computed [6] excitation function are shown in figure 4.2. The cross-section for the reaction employed in the present experiment can be seen in the same figure, and it is $\sim$ 10 nb. Eventually, in one week of running time, a total amount of 573 activities of interest, both for the short-lived and long-lived component, were collected.

4.2 RITU

After the target chamber, there is a mixture of fusion-evaporation products, scattered beam and target-like particles. This huge flux of particles would destroy immediately any silicon detector, hence it is necessary to separate the recoils from the primary beam. This separation is achieved via the Recoil Ion Transport Unit (RITU), which is a gas-filled separator with the optical configuration

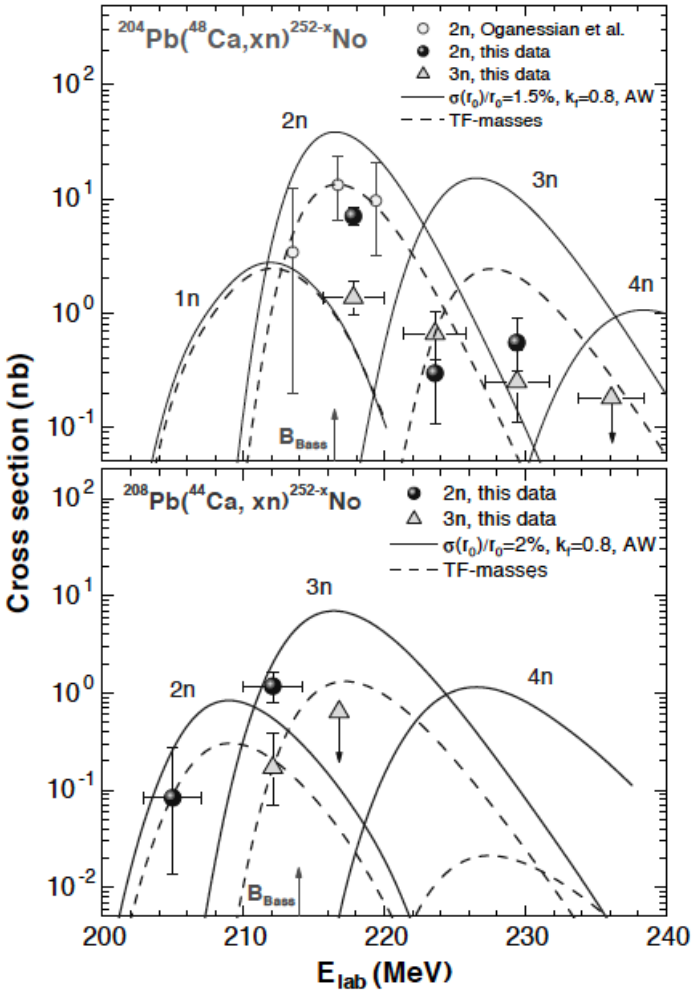

Figure 4.2: The production cross sections for the ^{48}Ca+^{204}Pb and ^{44}Ca+^{206}Pb, obtained in [2] and [3], for x*n* channels is illustrated with the dots, whilst the straight and dashed lines represent, correspondingly, the excitation functions calculated in [6]. Image taken from [3].

QDQQ shown in figure 4.3. The first magnet after the target chamber is a vertically focusing quadrupole (Q), followed by a separating dipole (D) and then by two focusing quadrupoles (QQ) [7]. This separator is typically filled with ~ 1 mbar of helium gas.

In a gas-filled separator, such as RITU, the transmission is very high, feature which is beneficial since we want to study typically low production cross-sections. After the fusion reaction, the recoils have a quite wide charge state distribution. During their flight through the separator they change their charge state several times, due to collisions with helium atoms, and they rapidly reach an average charge state of equilibrium. The recoil nuclei can be separated from the primary beam's particles because of their different magnetic rigidities. Partic-

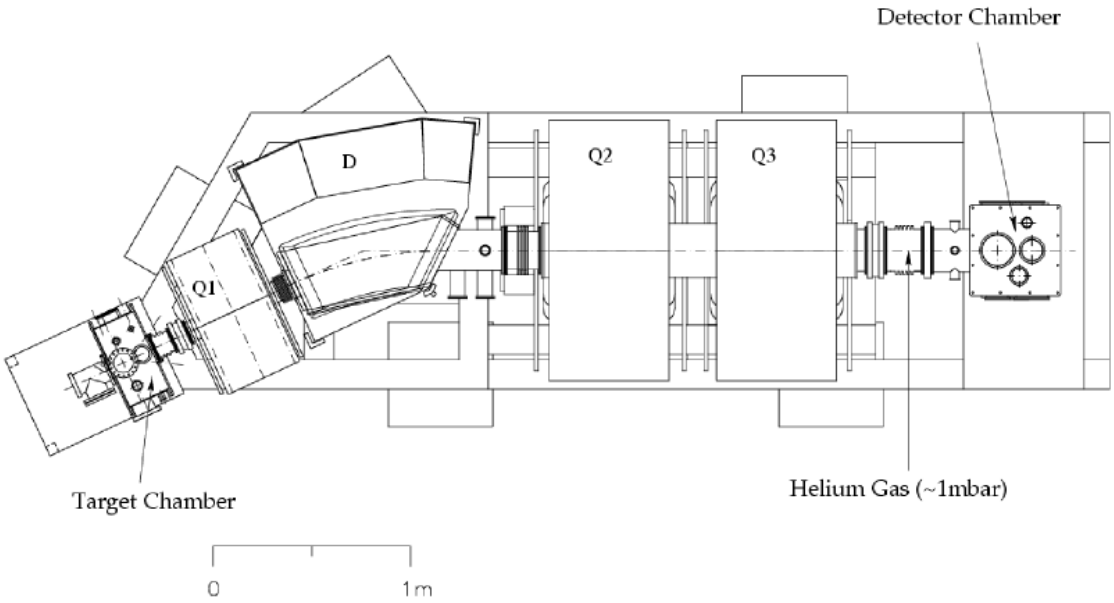

Figure 4.3: Schematic drawing of the gas-filled recoil separator RITU. The configuration is QDQQ, where Q stands for a focusing quadrupole magnet and D for a separating dipole magnet. Image taken from [26].

ularly, the magnetic rigidity is expressed as

$$B\rho = \frac{p}{q} \approx \frac{mv}{q_{ave}} \tag{4.1}$$

where B is the magnetic field strength and ρ is the radius of curvature. Also, p is the momentum, m the mass, E_k the kinetic energy and q is the equilibrium average charge.

4.3 Focal plane

At the focal plane there is the GREAT (Gamma Recoil Electron Alpha Tagging) spectrometer, which for the present study was composed of a multi-wire proportional counter (MWPC) and a double-sided silicon strip detector (DSSSD). A schematic view of the focal plane and the components described below can be observed in figure 4.4.

The main purpose of having the MWPC is to recognize between the recoils and their following decay products and between recoils and other lighter beam-like or target-like particles. This detector is filled with isobutane gas kept together with Mylar foils and it can only count the number of events without identifying

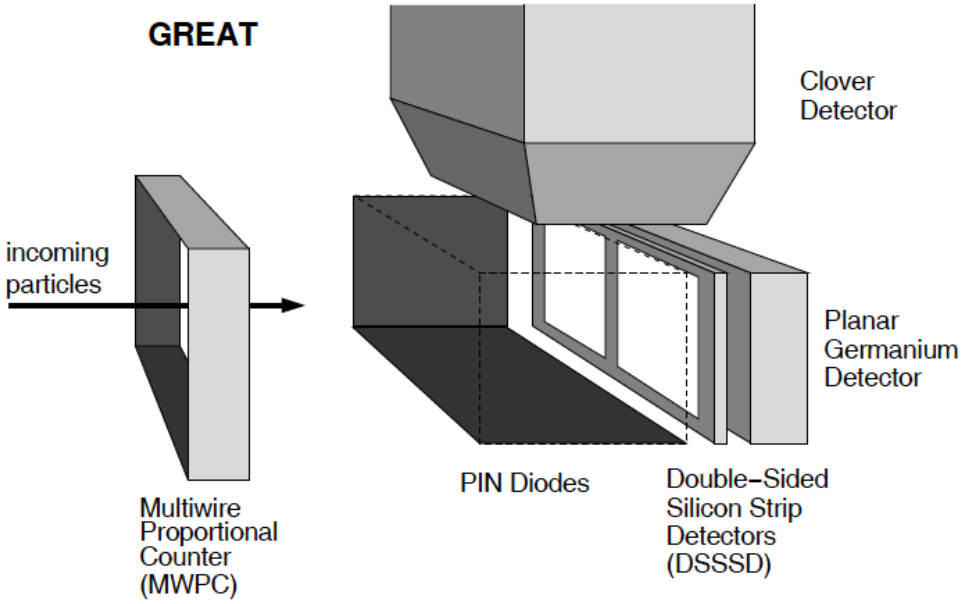

Figure 4.4: Schematic drawing of focal plane GREAT. Taken from [16].

their nature, exactly the same way a gas counter works. A charged particle going through it causes ionization and frees ions and electrons. These particles are accelerated and then collected on an electrode (the anodic or cathodic wires), creating an avalanche of ionization. When this occurs, the system detects that a recoil is approaching the DSSD and, doing so, records an energy deposition (happening in a specific pixel of the silicon detector and within a certain amount of time) as a recoil implantation. If this will be followed by another energy deposition, within the correlation time, we will observe a recoil-fission correlated event (figure 4.11 in the following section).

The DSSD is formed by two 300 μm thick silicon detectors. Each of these is made of 60 horizontal and 40 vertical 1 mm wide strips, for a total number of 4800 pixels. For this experiment, the vertical side of the DSSD was equipped with digital electronics, particularly with Lyrtech VHS-ADC cards, which allows to send the signal directly from the pre-amplifier to a flash ADC (Analog to Digital Converter). The horizontal side instead was instrumented with analogue electronics. The identification of the recoils of interest was made by requiring a signal in the MWPC in coincidence with an energy signal in the DSSD.

Recoil implantation events are correlated to subsequent decays in GREAT if they pass a ΔE-ToF gate, where ΔE refers to the energy deposition and ToF to Time of Flight. Imposing a gate to the fission fragments energy and the time difference between the recoil implantation and the fission event, we can correlate recoil and fission events. The result of this correlation, sliced on the two variables,

i.e. projected on the two axis, is given in figure 4.5.

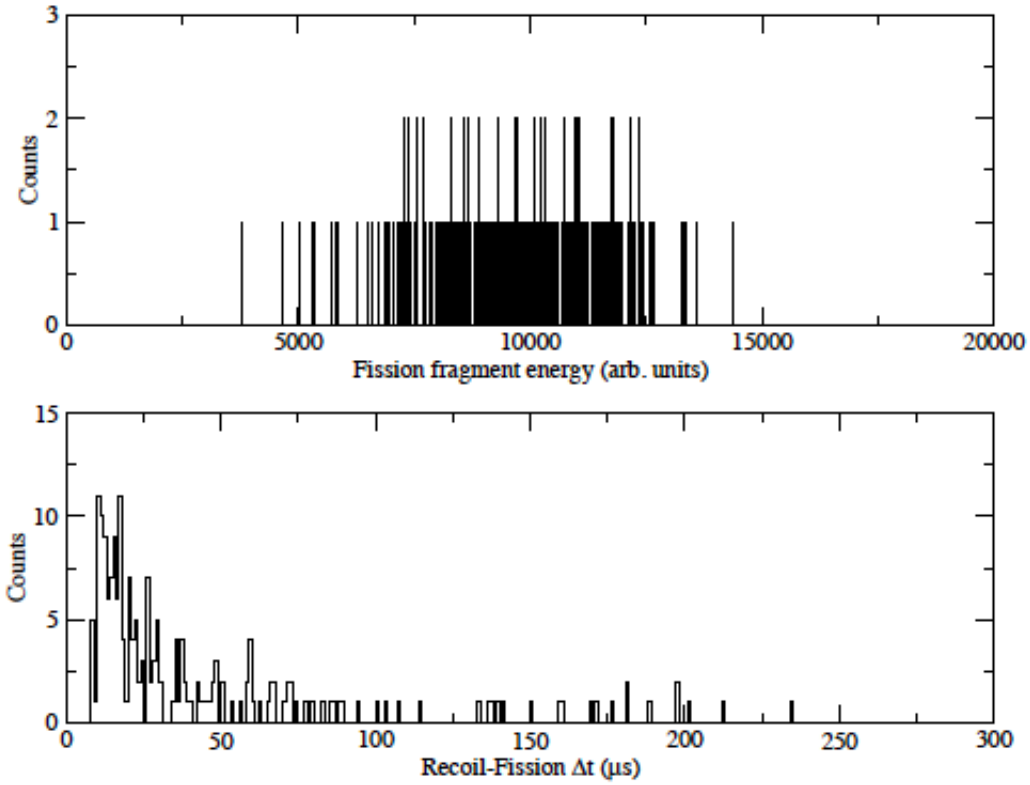

Figure 4.5: Fission fragments energy-Time of Flight gates projected, correspondingly, to x-axis (upper panel) and y-axis (lower panel).

Depending on whether the time difference between the recoil implantation and the fission event is larger or shorter than 8 μs, these events are recorded differently and processed with, correspondingly, analog or digital components. The main features of these two different systems is explained in the following section.

4.4 Data Acquisition System

In a radiation detection system the energy deposited in the detector is converted to charge and then passed to the pre-amplifier, whose output is a voltage step signal. In a conventional analog system this information is sent to a shaping amplifier, which returns a semi-Gaussian pulse that is fed to a ADC and then to the data analysis in the computers. This sequence is illustrated schematically in figure 4.6.

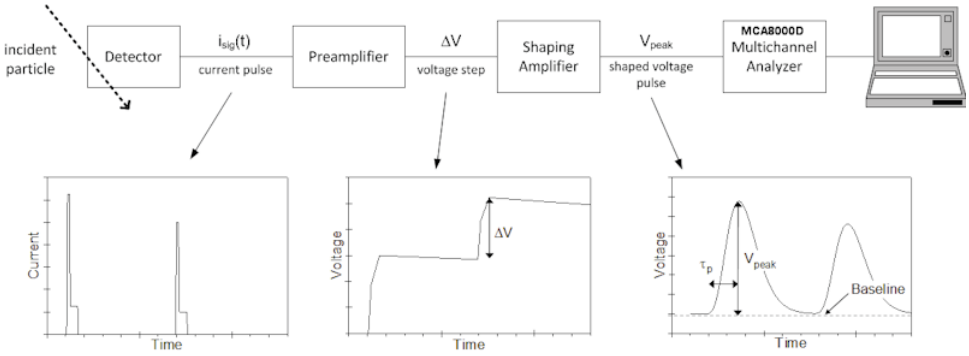

Figure 4.6: The steps leading from the energy deposited into the detector to analysis are illustrated, as well as the components responsible for each step of this sequence [28].

At the MCA (Multichannel Analyzer) input there is an ADC. The output of the shaping amplifier is an analog voltage signal which is digitized by the ADC and transformed into a discrete number, proportional to the signal amplitude. In other words, the ADC sorts the incoming pulses, according to their voltage, into a discrete number of channels.

The energy-channel relation is almost linear, so it can be approximated as:

$$E = a \cdot C + b \tag{4.2}$$

where E is the energy, a is the gain (energy per channel), C is the channel number and b is the offset.

The ADC and the DAQ (Data Acquisition System) are characterized by some parameters. One of these is the *dead time* and it refers to the time between the moment a signal enters the ADC and the one it arrives to the DAQ. If a pulse arrives to the ADC when the DAQ is still processing the previous one, this event cannot be recorded and is lost, representing a drawback in using conventional analog systems.

Another tricky aspect of the pulse-processing when using analog systems is the so-called pile-up. When a recoil implants in the detector it deposits its energy in it, and an event is registered. If a decay event follows the recoil implantation, also its energy is detected and, if this happens within a range of time (pre-defined by the user) and in the same pixel, these two events are correlated and the time difference between these two events is thus the decay time for that specific reaction product. If this time is under a certain threshold, the analog system is not able to resolve between the two consecutive events and pile-up occurs. A pile-up happens when two shaped signals overlap each other, causing the zero energy level of the second event to fall onto the tail of the first one. This results in a incorrect interpretation of the peak height and, hence, wrong determination of the energy. An illustration of pile-up event is shown in figure 4.7.

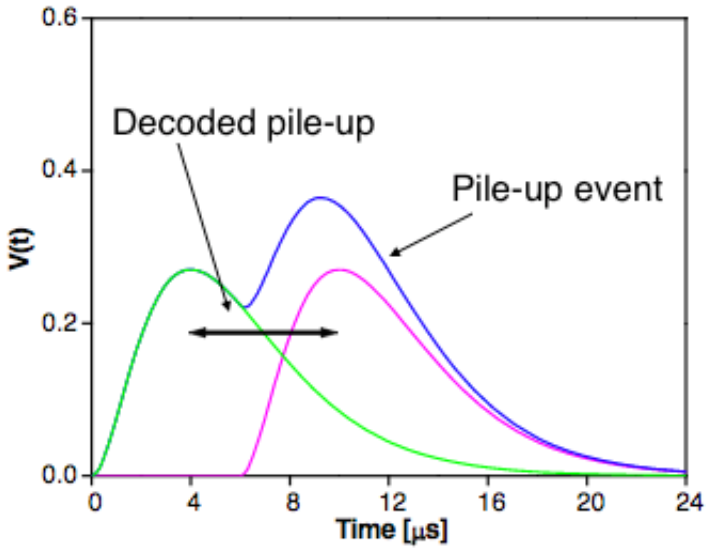

Figure 4.7: The *Decoded pile-up events* show the actual signals whilst the *Pulse pile-up events* show the output signal obtained. It is clear that the zero energy level for the overlapping signals, and therefore the deposited energy, is difficult to interpret correctly [29]

The problematics described above can be solved by using digital electronics. In this system, the energy deposited into the detector is sent directly from the preamplifier to a flash ADC, which is a high-speed multichannel acquisition platform, so that the pre-amplified signal is digitized directly. Therefore, the employment of digital electronics allows to detect pileup and correctly interpret the two overlapping signals. How information is passed from the detector to the computers in this kind of system is sketched in figure 4.8.

The digitization process and extraction of the pulse height can be seen in figure 4.8. The parameters needed to shape the output pulse are the peaking (and symmetrical falling) time Δt_L and flat top Δt_G. An average is calculated over the peaking and the falling time and these two averages are compared; their difference is plotted in order to create the trapezoid (see figure 4.8); this type of process is called *moving window deconvolution method* . In figure 4.9 there is a comparison between the analog and digital shaping outputs.

A useful tool resulting from the use of digital electronics is the so-called *trace*, which is digitized representation of the pre-amplified signal as previously explained. Practically, a trace is a plot with deposited energy on the y-axis, plotted against relative time on the x-axis. In our case, on the x-axis each bin corresponds to 10 ns, and the range is set to go from 0 to 1024 bins, i.e. from 0 ns to 10240 ns. For this experiment, in order to record a trace, we requested that the recoil pulse height fell in a well-defined energy range (fission fragments energy)

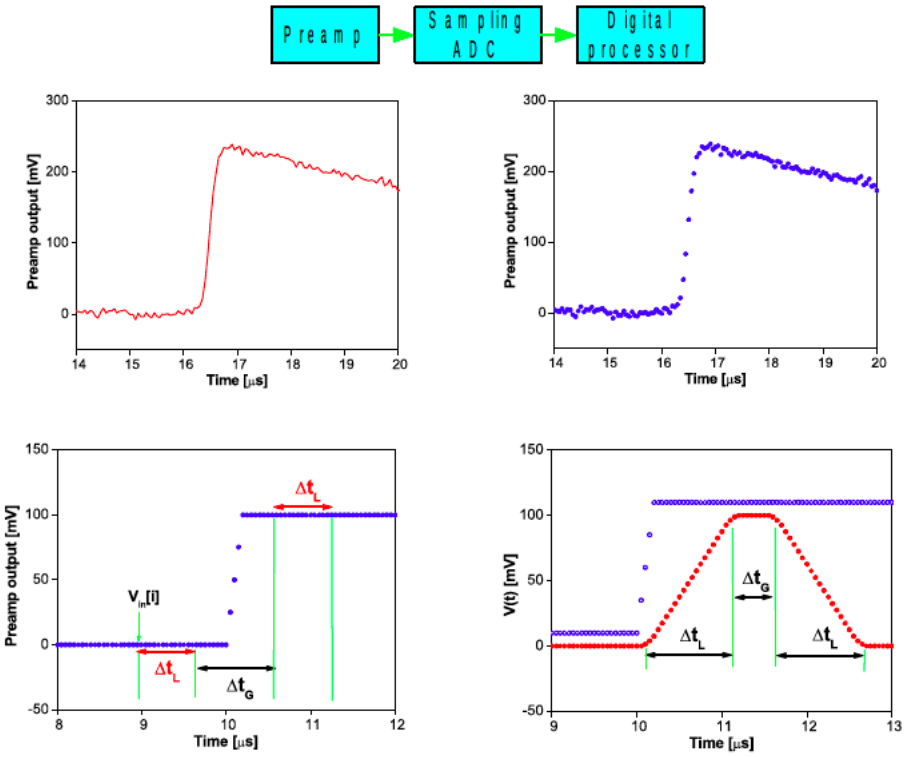

Figure 4.8: Sequence illustrating the digitalization process for a pulse to obtain the trapezoid shape. In the output pulse there is Δt_L peaking time and a symmetrical fall time and a flat top of Δt_G [29].

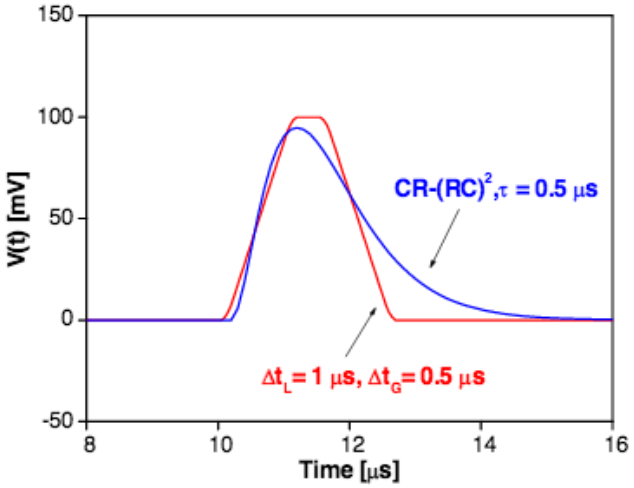

Figure 4.9: Comparison between analog filter with τ=0.5μs, with peaking time 2τ and total width of about 6τ, and digital filter with Δt_L=1μs and Δt_G=0.5μs [29].

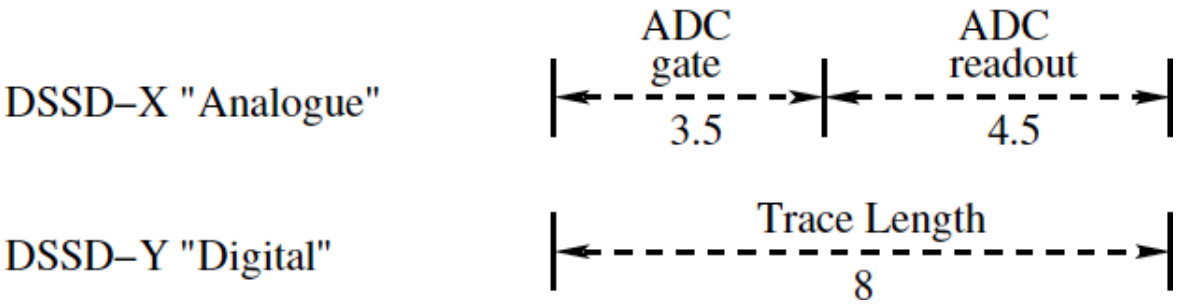

Figure 4.10: Comparison between processing times for analogue (upper panel) and digital (lower panel) systems.

and that the forming fission trace went over scale, because of the gain of the pre-amplifier. If both these conditions were satisfied the system created a trace. More details about the use of traces will be given in section 5.2.

A direct comparison between the analog and the digital processing times is shown in figure 4.10. In the analogue system, recoil and fission events can not be resolved if they occur within 8 μs, because the fission would happen while the system would still be processing the preceding recoil signal. The digital electronics, on the other hand, are able to detect and record both the recoil and the fission, which now belong to the same event, indeed, the *trace*. In case instead recoil and fission occur with a time difference longer than 8 μs, the DAQ is able to resolve between them, correlate them if they happen in the same pixel, record the time difference and save it as a decay time. This kind of correlation is illustrated in figure 4.11.

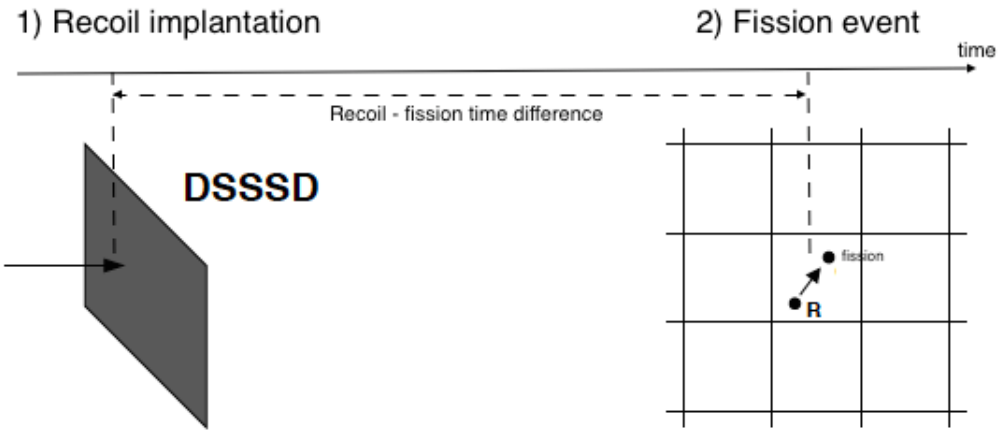

Figure 4.11: Correlated recoil implantation and fission events. This distinction can be performed if the time difference is larger than 8 μs, otherwise the two events are recorded as only one trace by the digital electronics.

Chapter 5

Data analysis

The data collected during this experiment were analyzed with a Total Data Readout (TDR), which is a trigger-less data acquisition system which reads every channel asynchronously in single mode. The software used to sort the TDR raw data stream was *Grain* [23], developed by Panu Rahkila, University of Jyväskylä.

5.1 Presence of electromagnetic branch

The first point of the data analysis was to answer the puzzling question about the origin of the long-lived activity detected, in this study as well as in the previous ones (see chapter 2). The goal was to understand whether the isomeric state undergoes direct fission, with longer half-life than the ground state, or it electromagnetically decays to the ground state, which then fissions.

In order to do so, we looked for recoil-electron-fission correlated events, which means we looked for correlations between a fission event observed on the X-side of the DSSD and an electron observed on the Y-side and a signal from the MWPC, happening within a time and in the same pixel of the DSSD. A total number of 23 correlated events was observed, proving the presence of an electromagnetic branch. These events are shown in figure 5.1. Also, we found the the recoil-electron time difference is always long, compared to the electron-fission which is always short. This implies that the longer lived activity belongs to the isomeric state.

5.2 Short-lived component

The search for the ground-state fission events was firstly done using the digital electronics, which allowed to record digitized traces of the pre-amplified signals

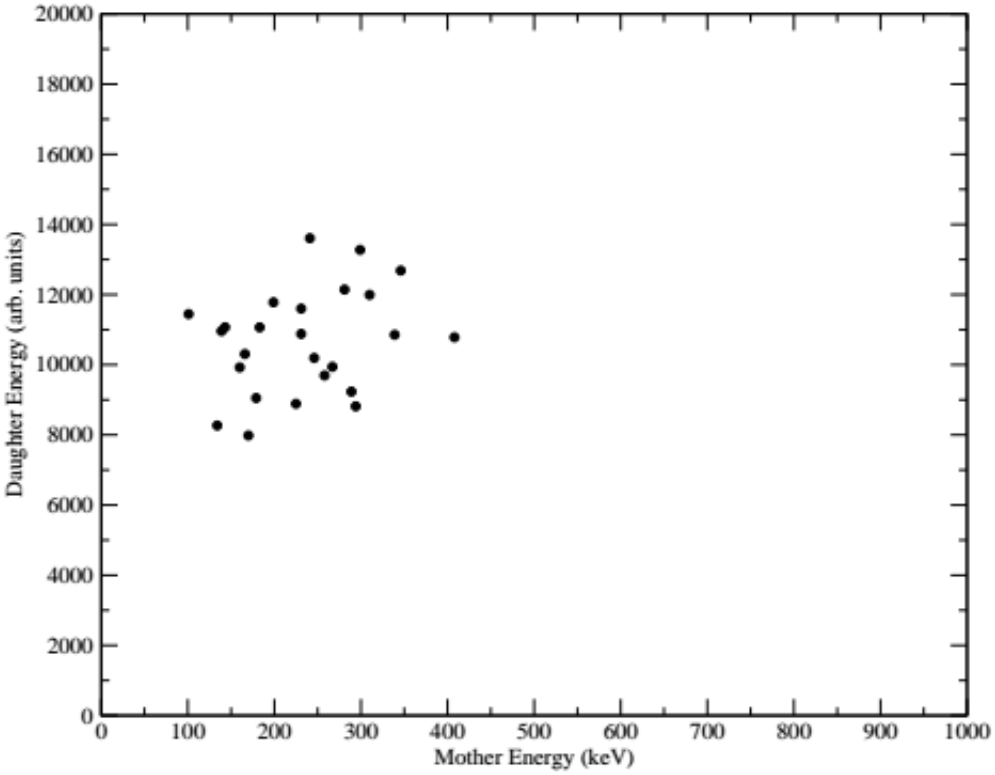

Figure 5.1: Correlated recoil-electron-fission events. The three events are recorded as different events and their time difference is required to be bigger than 8 μs.

(see section 4.4). Example traces for recoils implantations followed by a fission event below a time difference of 8 μs can be seen in figure from 5.2 to 5.4. To be noticed that now implantation and fission are recorded by the system as one event. The maximum length of the trace is up to 8 μs after the implantation.

The first "jump" in the trace happens always at $\sim$ 1700 ns because there is an offset in the electronics, aimed to facilitate the analysis. The second jump corresponds to a following signal, specifically a fission event. The time between these two energy depositions in the detector is the decay time of that specific implanted nucleus.

Overall, 377 traces of interested were collected. The decay time of each trace is calculated via a sorting code based on the moving window deconvolution method. The code calculates the average over 100 ns and over the next 100 ns interval, it compares them and it moves on in case there is no drop. Where a "jump" occurs, i.e. when two consecutive averages differs for a large amount, the system records the time at which this jump occurred. It then proceeds analogously until the end of the trace or until a second jump is detected. In case

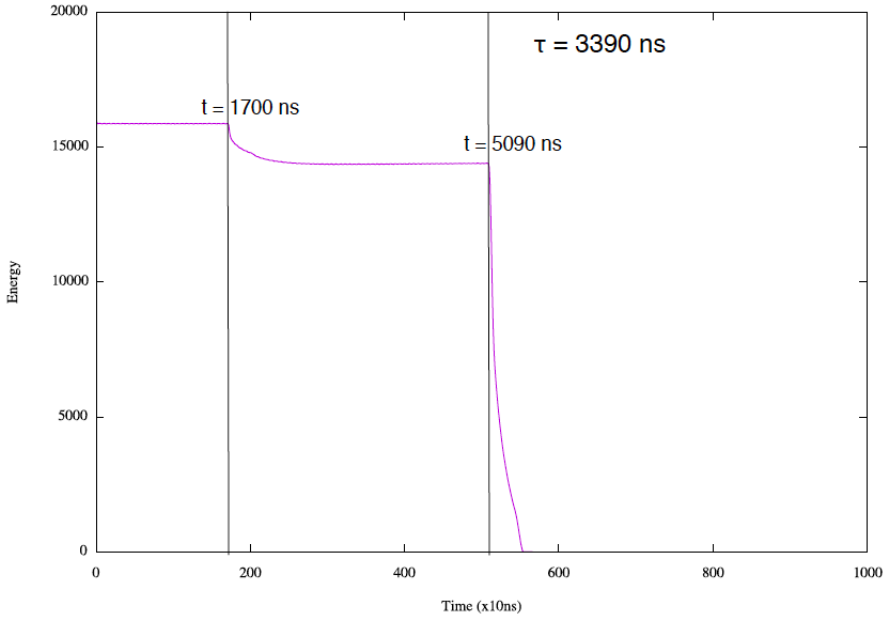

Figure 5.2: Example of digitized trace for a recoil implantation that happened at t=1700 ns followed by a fission event at t=5090 ns. This corresponds to a life time $\tau = 3.39 \pm 0.01 \mu s$. The implantation time is at t=1700 ns and not at t=0 ns because of the presence of an offset in the electronics, aimed to facilitate the analysis.

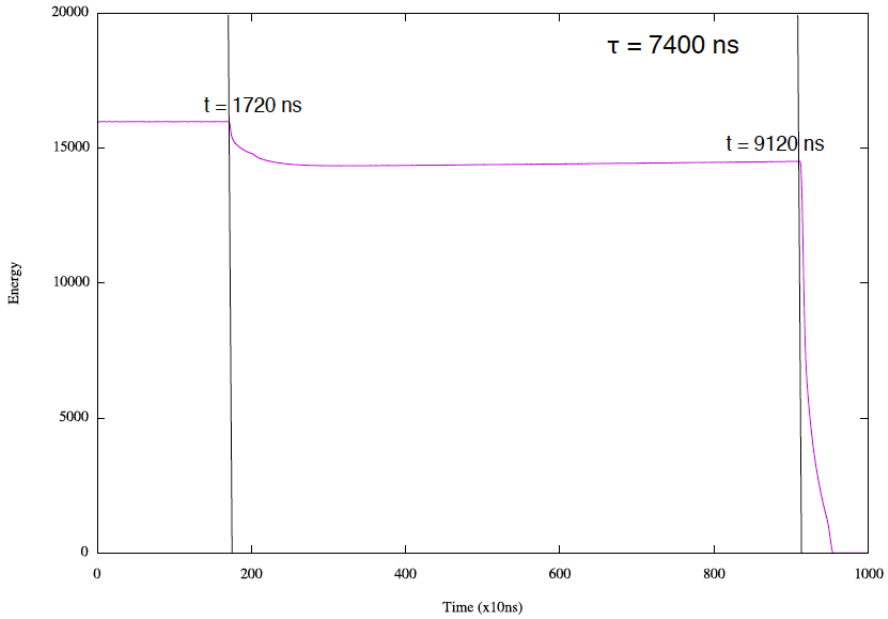

Figure 5.3: Example of digitized trace for a recoil implantation that happened at t=1720 ns followed by a fission event at t=9120 ns. This corresponds to a life time $\tau = 7.40 \pm 0.01 \mu s$. The implantation time is at t=1700 ns and not at t=0 ns because of the presence of an offset in the electronics, aimed to facilitate the analysis.

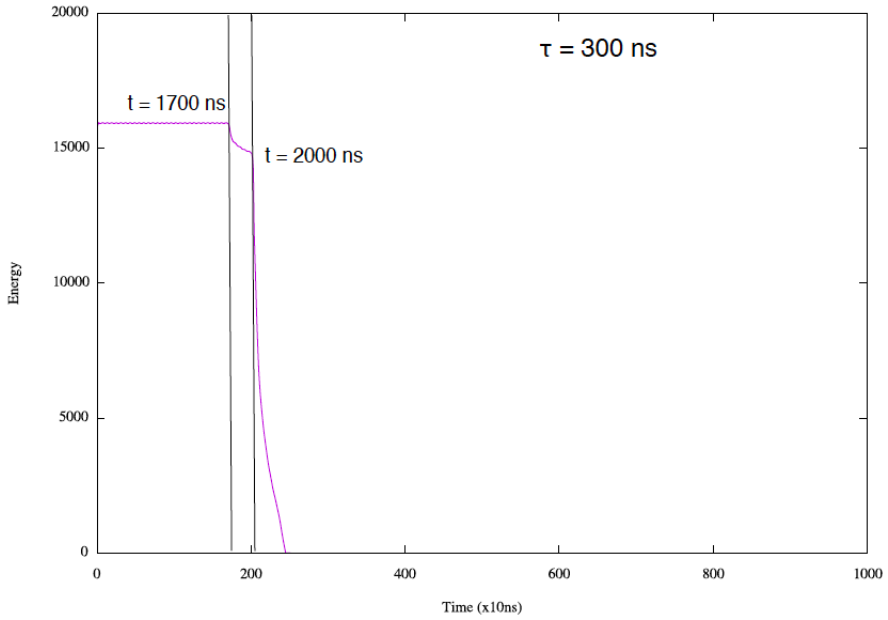

Figure 5.4: Example of digitized trace for a recoil implantation that happened at t=1700 ns followed by a fission event at t=2000 ns. This corresponds to a life time $\tau = 0.30 \pm 0.01 \mu s$. The implantation time is at t=1700 ns and not at t=0 ns because of the presence of an offset in the electronics, aimed to facilitate the analysis.

there is a second jump it calculates and stores the difference between these two times.

At first, the life-time of the short-lived activity was calculated from the decay times extracted from the traces using the maximum likelihood method, i.e. computing the average of all of them. The upper and lower limit of the error bar were calculated, correspondingly, via the relations

$$\tau_u \cong \frac{\overline{t_m}}{1 - \frac{z}{\sqrt{n}}} = 1,054 \times \overline{t_m} \tag{5.1}$$

and

$$\tau_l \cong \frac{\overline{t_m}}{1 + \frac{z}{\sqrt{n}}} = 0,951 \times \overline{t_m} \tag{5.2}$$

where z is taken to be 1 for standard errors, $\overline{t_m}$ is the average of the decay time and n is the number of counts [15].

With this kind of preliminary analysis the life-time was found to be

$$\tau = 3.3 \pm 0.2\ \mu s \tag{5.3}$$

corresponding to a half-life of

$$t_{1/2} = 2.3 \pm 0.1\ \mu s. \tag{5.4}$$

5.3 Long-lived component

The data relative to recoil-fission correlated events for which the time difference was greater than 8 μs, were also collected. Now the DAQ is able to resolve between the two events, and the time difference between these two is the decay time. A total amount of 196 events of this type were detected. Out of this number, 143 events have a decay time in the range $8\mu s < \tau < 50\mu s$ while the other 53 events showed decay time in the region 50-300 μs. All these results can be seen in figure 5.5.

These results were fitted to the exponential decay curve expressed in equation 3.1, in order to estimate the corresponding half-life. From this fitting, the decay constant resulted to be

$$\lambda = 0.021 \pm 0.003\ \frac{decays}{\mu s} \tag{5.5}$$

Using relations in equation 3.2 leads to the results:

$$\tau = 49 \pm 7\ \mu s \tag{5.6}$$

and

$$t_{1/2} = 34 \pm 5\mu s \tag{5.7}$$

A careful observation of the slope of the curve and of the distribution of the events, suggests that in the 8-300 μs region we are observing many events which actually belong to the short-lived activity.

A rough calculation based on the half-life expressed in equation 5.4, leads to assume that after $\sim 20\mu s$ almost all of the nuclei belonging to the short-lived activity should have been decayed. More precisely, since according to the calculation 5.4 half of them decay every $2,3\mu s$, after 20 μs there should be less than 1% of the short-lived nuclei left. On the basis of what just explained, in order to extrapolate the half-life of the long-lived activity, a possibility could be to apply

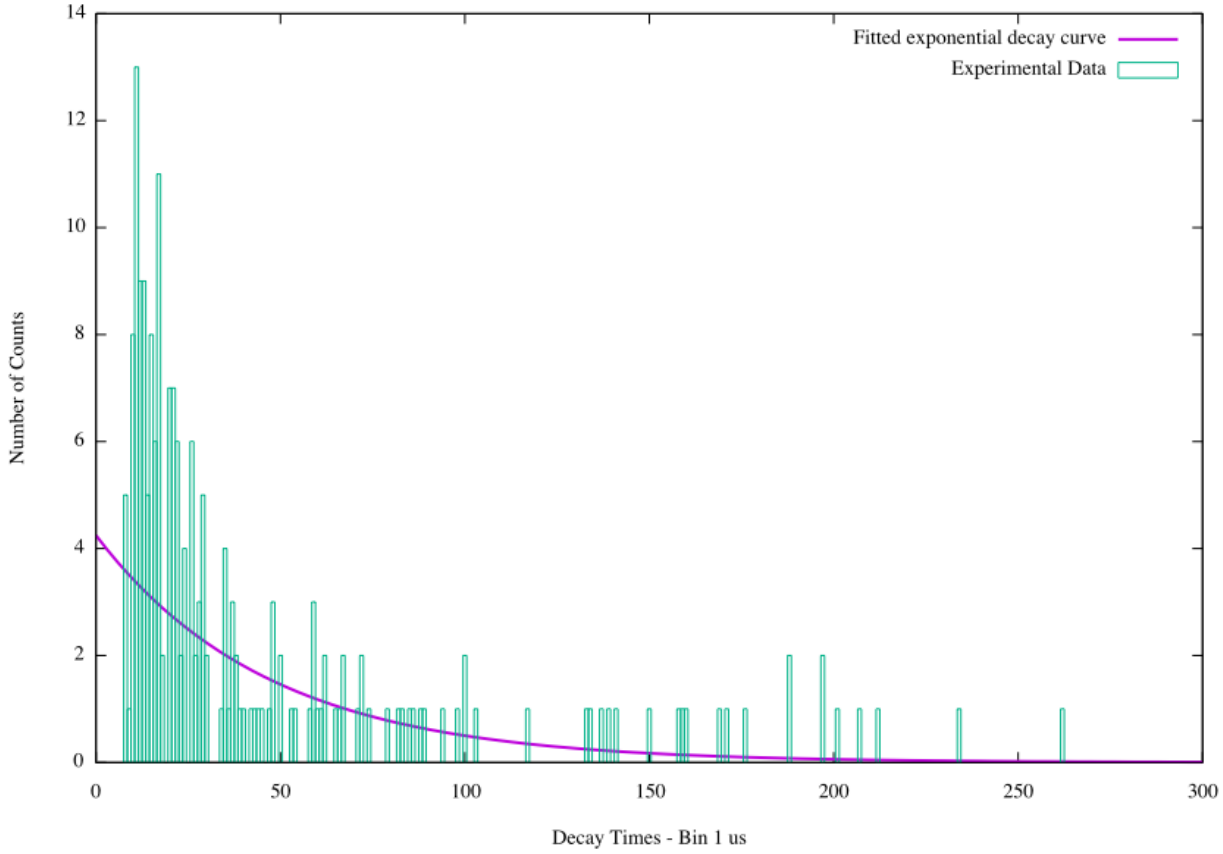

Figure 5.5: Correlated recoil-fission events with decay time between 8 and 300 μs (green) and fitting (purple). The bin is 1 μs. The exponential decay law was fitted to the experimental results.

the Maximum Likelihood Method on the events with decay time between 20 and 300 μs. Performing this calculation, the results were:

$$\tau = 84^{+9}_{-7}\mu s \tag{5.8}$$

and

$$t_{1/2} = 58^{+6}_{-5}\mu s \tag{5.9}$$

This half-life is significantly longer than the one in 5.7, but this should not surprise. The same calculation that led to choose $20\mu s$ as a limit for which beyond we do not expect more than 1% of the short-lived activity events, can be applied now for the long-lived nuclei. Considering the half-life in 5.7, since half of the isomers will decay in 34 μs, we expect that a non negligible part of them will have decayed before $20\mu s$.

The discrepancies between the results obtained with the aid of the MLM (20-300 μs time range) and by the fitting procedure (over 8-300 μs time range) rep-

resent a clear evidence of the fact that is necessary to find a way to clearly distinguish the two components. Therefore, it became necessary to combine both type of events in the same set of data, in order to observe a full range 0-300 μs.

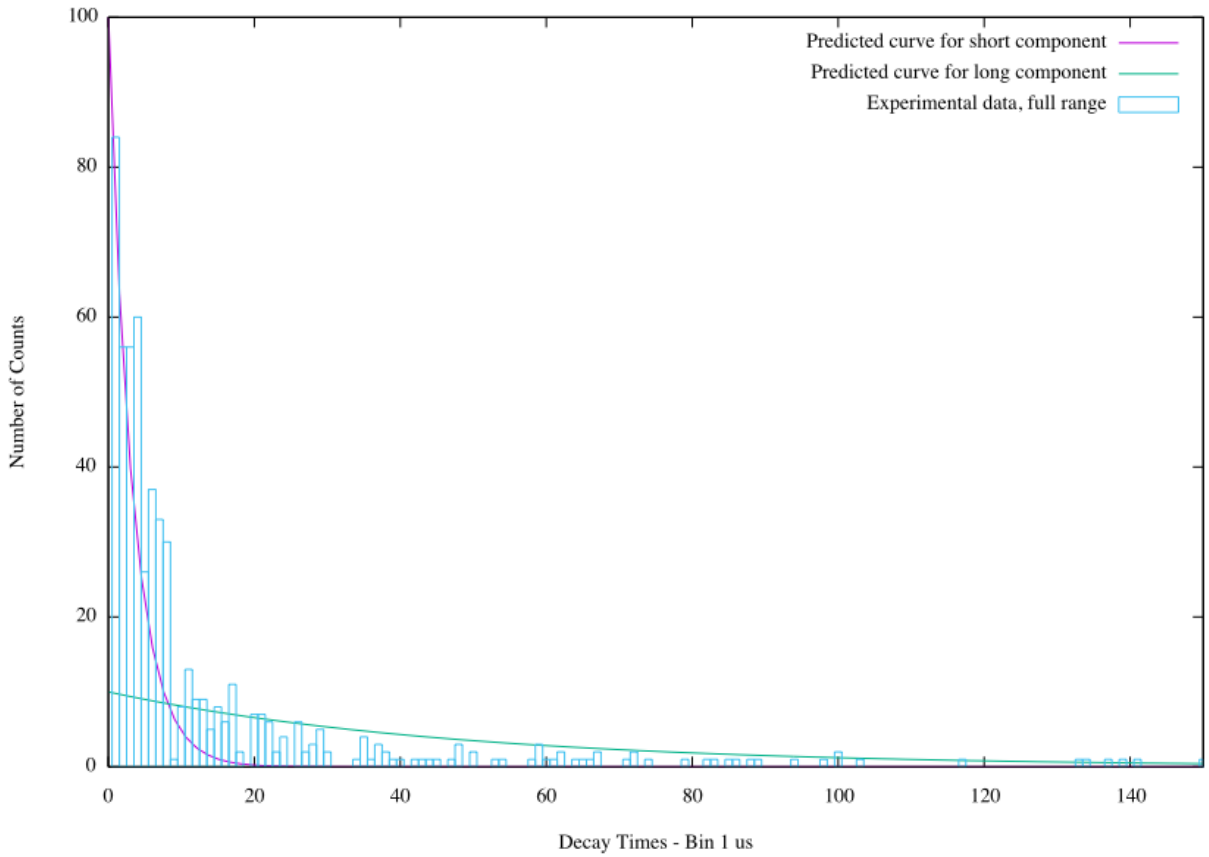

Figure 5.6: Full time-range of the fission decay events, showing both the short and the long component (blue boxes). The purple line is the decay curve for the result obtained in section 5.2 while the green line represents the fitting shown in figure 5.5. The scale on the x-axis was limited to 0.150 μs in order to visualize better the region of major interest.

Figure 5.6 shows the full set of data collected together with the decay curves obtained plugging into equation 3.1 the results of the current and the previous section. Given that the two components co-exist strongly in the region around the border in 8 μs, an accurate fit is not possible and a method to separate them was needed.

5.4 K.H.Schmidt Method for separating long and short component

In order to effectively distinguish between the two different components, a possible approach is to apply to the case of the present work the method proposed by K.H.Schmidt in [8] in order to recognize random events in an exponential distribution. The basic idea is to plot a logarithmic time scale on the x-axis, instead of the usual times. Doing this, the exponential curve becomes a bell-shaped curve with a tail on the left-hand side, and in case there are two different components two separate bells can be observed. An example of this plot can be seen in figure 5.7 [8].

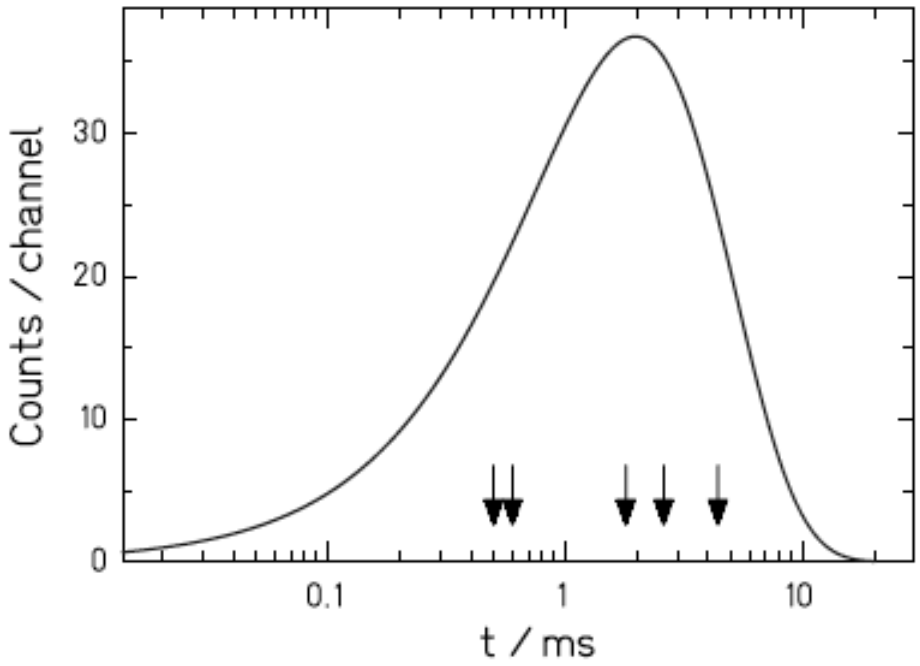

Figure 5.7: Example of logarithmic scale decay-time distribution. This particular decay distribution refers to five α-decay events of $^{271}110$. Image taken from [8].

The expression for this kind of curve can be found starting from equation 3.1 [8]. Calculating the derivative of this relation gives:

$$\left|\frac{dn}{dt}\right| = \lambda n_0 \exp(-\lambda t) \tag{5.10}$$

Rearranging the derivative in equation 5.10, it is possible to write:

$$\begin{aligned} \frac{dn}{d(\ln t)} = \frac{dn}{dt}\frac{dt}{d(\ln t)} = -n_0 \lambda t \exp(-\lambda t) = \\ = -n_0 \exp(\ln(\lambda t)) \exp(-\exp(\ln(\lambda t))) = \\ = -n_0 \exp(\ln t + \ln \lambda) \exp(\exp(-\ln t + \ln \lambda)) \end{aligned} \tag{5.11}$$

Denoting $\theta = \ln t$, the curve described above can be written as

$$\left|\frac{dn}{d\theta}\right| = n_0 \exp(\theta + \ln \lambda) \exp(-\exp(\theta + \ln \lambda)) \tag{5.12}$$

This bell-shaped curve has a maximum when

$$\frac{d^2 n}{d\theta^2} = 0 \rightarrow \theta_{max} = \ln(\frac{1}{\lambda}) \tag{5.13}$$

Therefore, the aim is to fit experimental data to this function. Particularly, knowing already that two different components co-exist in these data, the fit needs to be done to two different functions, with decay constants λ_l and λ_s , correspondingly for the long and the short component.

The result of this fitting is shown in figure 5.8. The blue boxes are the experimental data in logarithmic time-scale. The red and the green lines are the fittings of functions of the type of 5.12, correspondingly for the short-lived and the long-lived components, while the yellow line is simply the sum of the two components. Fitting the curve to the experimental data allowed to find the parameters λ_l and λ_s, from which the life-time τ and the half-life $t_{1/2}$ could be derived using the relations 5.13 and 3.2. The results obtained are summarized in table 5.1.

Table 5.1: Results of present work for decay constant, life-time and half-life for both ground-state and isomer.

Quantity	**Isomeric State**	**Ground State**
λ	$0.023 \pm 0.004 \ \frac{decays}{\mu s}$	$0.207 \pm 0.014 \ \frac{decays}{\mu s}$
τ	$44 \pm 8 \ \mu s$	$4.8 \pm 0.3 \ \mu s$
$t_{1/2}$	$31 \pm 5 \ \mu s$	$3.4 \pm 0.2 \ \mu s$

To sum up, the half-life of the ground-state was found to be $t_{1/2}(g.s.) = 3.4 \pm 0.2 \mu s$, while the half-life of the isomeric state was calculated to $t_{1/2}(i.s.) = 31 \pm 5 \mu s$.

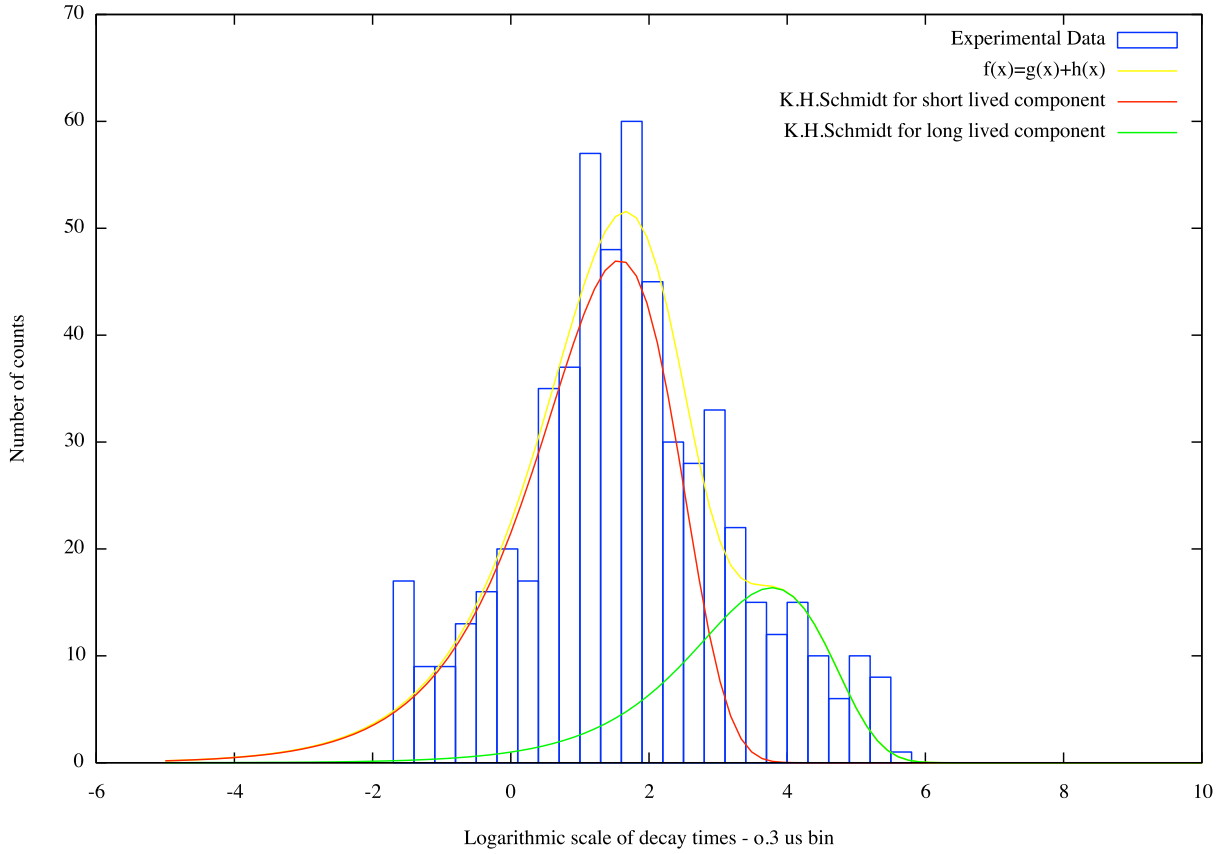

Figure 5.8: Logarithmic time scale for detected short and long component (blue boxes), together with fitting curves (red line for short-lived component and green line for long-lived component).

Once the two components had been separated, it was possible to integrate the two distributions in order to find a cross-section ratio, between the production cross-section of the ground state and the one of the isomeric state. This resulted in $\sigma_{short}/\sigma_{long} \approx 2.87$, showing that among all the fusion reactions happening, around 26% of them feeds the isomer while the remaining ones feed the ground-state.

Chapter 6

Results and discussion

Comparing the results of the present work with the most recent ones about the decay of ^{250}No, we can state that important steps forward have been taken. We were able to answer the puzzle left open by Peterson [4] by proving the presence of an electromagnetic branch from the isomeric to the ground state. Doing so, we proved that the longer activity has to be attributed to the fission of the isomer, which was not directly fed by the fusion reaction but, instead, from the decay of the isomeric state.

Also the half-life measurements are in good accordance with the older results. More specifically, the half-life of the ground-state that has been derived in this work matches precisely the one calculated by Peterson [4]. The half-life of the isomeric state seems to be shorter than the one previously obtained, but still it is within the uncertainty range, therefore maintaining agreement between the two measurements. For both the short and the long component the accuracy was improved significantly.

To understand the observed difference between the short half-life calculated from the full set of data (section 5.4) and the one calculated from the digitized traces (section 5.2), it is important to focus on what happens around the 8 μs border.

Firstly, integrating the short component curve for $\tau > 8\mu s$, i.e. for $\theta = \ln(\tau) > 2.01\mu s$, we found that $\sim$20% of these events lay in that region, which means that they are not taken into account by the analysis of traces, discussed in section 5.2. In other words, when calculating the average of the decay times extracted from the traces, we are not including the longer-lived nuclides and hence we are obtaining a shorter life-time. Similarly, for the same reasons expressed above, applying the Maximum Likelihood Method to the 20-300 μs results in a half-life of the isomeric state which seems longer than the one calculated from the complete set of data.

Secondly, from figure 5.8 a drop in the number of counts around $\ln(\tau) \sim 2.1\mu s$ can be clearly seen. The most likely explanation for this discontinuity is related to the fact that, searching for correlations within 8 μs and then time differences greater than 8 μs, probably causes a loss of those data for which the recoil-fission time difference is exactly around this 8 μs threshold. These two facts explain why the half-life extrapolated from the traces is shorter than the one obtained when considering the full time-range.

We can state that the goal of the work has been successfully achieved. The origin of the two different activities previously observed has been clarified by the presence of an electromagnetic branch and the two half-lives have been measured.

One possible development could be to investigate into the rotational band leading from the 6^+ isomer to the 0^+ ground-state, since so far we just proved the existence of an electromagnetic branch. Also, the even-even neighbor ^{248}No is not known and one could think to extend the research to that. Given the behavior of the fission half-life for nuclei in this region (see figure 2.1) and how it drops when going far from N=152, hence ^{254}No for Z=102, the fission barrier could disappear completely when going to ^{248}No, and this would be a very interesting topic to cover in order to understand fully the behavior of isotopes around the N=152 shell.

Bibliography

[1] G.M. Ter-Akopyan, A.S. Iljinov, Yu. Ts. Oganessian, O.A. Orlova, G.S. Popeko, S.P. Tretyakova, V.I. Chepigin, B.V. Shilov, G.N. Flerov, Nucl. Phys. A 255, 509, (1975)

[2] Yu.Ts. Oganessian, V.K. Utyonkov, Yu.V. Lobanov, F.Sh. Abdullin, A.N. Polyakov, I.V. Shirokovsky, Yu.S. Tsyganov, A.N. Mezentsev, S. Iliev, V.G. Subbotin ıet al., Phys. Rev. C **64**, 054606 (2001)

[3] A.V. Belozerov, M.L. Chelnokov, V.I. Chepigin, T.P. Drobina, V.A. Gorshkov, A.P. Kabachenko, O.N. Malyshev, I.M. Merkin, Yu.Ts. Oganessian, A.G. Popeko ıet. al, Eur. Phys. J. A 16, 447-456 (2003)

[4] D. Peterson, B.B. Back, R. V.F.Janssens, T.L. Khoo, C.J. Lister, D.Seweryniak, I. Ahmad, M.P. Carpenter, C.N. Davids, A.A. Hecht ıet. al, Phys. Rev. C 74, 014316 (2006)

[5] F.G. Kondev, G.D. Dracoulis, T. Kibédi, Atomic Data and Nuclear Data Tables 103-104 (2015) 50-105

[6] W. Reisdorf, Z. Phys. A 300, 227 (1981); W. Reisdorf, M. Schädel, Z. Phys. A 343, 47 (1992)

[7] J. Sarén, J. Uusitalo, M. Leino, J. Sorri, Nucl. Instr. Methods Phys. Res. A 654, 508 (2011)

[8] K.H. Schmidt, Eur. Phys. J. A 8, 141-145 (2000)

[9] J. Pakarinen, P. Papadakis et al., *The SAGE spectrometer*, The European Physical Journal A, March 2014, 50:53

[10] J.P. Delaroche, M. Girod et al., Nuclear Physics A 771, 103 (2006)

[11] S. Vandenbosch and P. Day, Nuclear Physics 30, 177 (1961)

[12] E.-M. Franz, S. Katcoff *et al.*, Phys. Rev. C 23, 2234 (1981)

[13] M. Goeppert-Mayer, Phys. Rev. 78 (1950)

[14] A. Abel-Hafiez, Physics Journal, Vol. 1, No. 1, July 2015

[15] Matti Leino, *Lectures on low statistics*, 2003

[16] Steffen Ketelhut, *Rotational Structures and High-K Isomerism in $^{248,250}Fm$*, PhD Thesis, 2010

[17] Carl Wheldon *K-isomerism at high-spin beyond the fusion limit*, PhD Thesis, 1999

[18] Ali Al-Khatib, *High-Spin γ-Ray Spectroscopy of ^{124}Ba, ^{124}Xe and ^{125}Xe.*, PhD Thesis, 2009

[19] Kenneth S. Krane (1988), *Introductory Nuclear Physics*

[20] Richard F. Casten (1990), *Nuclear structure from a simple perspective*

[21] https://universe-review.ca/I14-03-potential.jpg

[22] http://shodhganga.inflibnet.ac.in/bitstream/10603/8725/7/07_chapter_2.pdf

[23] https://trac.cc.jyu.fi/projects/grain/wiki/GrainDocs

[24] http://www.wiley.com/legacy/products/subject/physics/toi/toi.pdf

[25] https://web-docs.gsi.de/~wolle/ISOMER/isomer.html

[26] https://www.jyu.fi/fysiikka/en/research/accelerator/nucspec/RITU

[27] https://www.jyu.fi/fysiikka/en/research/accelerator/nucspec/jurogam/photos/drawings/great-jurogam-2.jpg

[28] http://www.amptek.com/products/mca-8000d-digital-multichannel-analyzer/

[29] https://www.science.mcmaster.ca/medphys/images/files/courses/4R06/4R6Notes6_Pulse_Processing.pdf

[30] http://isotopes.lbl.gov/toimass.html